Materials & Design 260 (2025) 114969

Contents lists available at ScienceDirect

Materials & Design

journal homepage: www.elsevier.com/locate/matdes

3D viscoelastic plastic model coupled with a continuum damage formulation for fiber reinforced polymers

Johannes Gerritzen [a,*], Benjamin Gröger [a], Matthias Zscheyge [b], Andreas Hornig [a,c,d], Maik Gude [a]

[a] TUD Dresden University of Technology, Institute of Lightweight Engineering and Polymer Technology (ILK-TUD), Holbeinstr. 3, 01307 Dresden, Germany
[b] Fraunhofer Institute for Microstructure of Materials and Systems IMWS, Walter-Hülse-Straße 1, 06120 Halle, Germany
[c] Center for Scalable Data Analytics and Artificial Intelligence (ScaDS.AI) Dresden/Leipzig, TUD Dresden University of Technology, Strehlener Str. 14, 01069, Dresden, Germany
[d] Department of Engineering Science, Solid Mechanics and Materials Engineering, University of Oxford, OX1 3PJ, Oxford, United Kingdom

HIGHLIGHTS

- 3D constitutive model for unidirectionally reinforced thermoplastics.
- Differentiation between continuum damage, plasticity and viscoelasticity.
- Full parameter identification for developed model on glass fiber reinforced polypropylene at 1.1e-4 1/s.
- Model verification under various loading conditions at several strain rates up to 2.2e-2 1/s.
- Validation by low velocity impact experiments at 4.5 and 6.0 m/s without parameter adaptation.

GRAPHICAL ABSTRACT

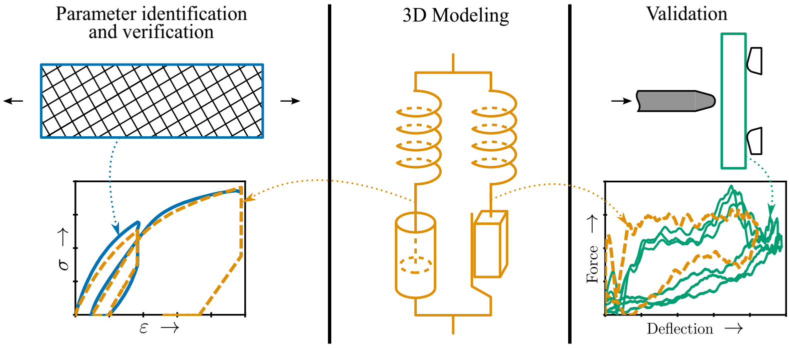

ARTICLE INFO

Keywords:
Fiber reinforced polymers
Constitutive modeling
Continuum damage mechanics
Plasticity
Strain rate dependency
Low-velocity impact

ABSTRACT

Fiber reinforced polymers with thermoplastic matrices are increasingly used in diverse applications. As a result, ever more complex loading conditions have to be considered in their design. To improve the predictive capabilities, a recently proposed constitutive model for fiber reinforced thermoplastic (FRT), originally formulated for two dimensional (2D) loading conditions, is extended to general three dimensional (3D) loading. The model accounts for stiffness degradation, inelastic deformation as well as strain rate dependency. A comprehensive derivation of the constitutive equations is presented in combination with adaptations for unidirectionally reinforced (UD) composites, which does not necessitate introducing additional model parameters. The resulting 3D-model is validated at coupon level using quasi-static and low-velocity impact experiments. It is shown that the model generalizes well to complex loading conditions and various strain rates.

1. Introduction

1.1. Motivation

The importance of FRTs continues to grow, primarily driven by advantageous properties of the matrix compared to established thermoset resins: Firstly, their ductility leads to a more progressive failure behavior, significantly improving a structure's performance under impact [1] or crash [2,3]. Secondly, the ability to melt the matrix facilitates its processing, enabling forming [4] and novel joining technologies for composites [5,6] whilst improving their recyclability [7].

---

[*] Corresponding author.
Email address: johannes.gerritzen@tu-dresden.de (J. Gerritzen).

https://doi.org/10.1016/j.matdes.2025.114969
Received 30 July 2025; Received in revised form 25 September 2025; Accepted 16 October 2025

Since such applications are characterized by intricate process-structure-property interactions, their development can pose significant challenges. Numerical simulations offer a promising approach to accelerate them and improve robustness [8,9], even enabling analyses with focus on sustainability [10] and recyclability [11] at an early stage.

For a reliable simulation-aided development process of FRTs based lightweight structures, the resulting load bearing behavior has to be predicted. This necessitates taking the resulting 3D material structure and corresponding mechanical behavior into account. Such a description is very challenging for FRTs, since several effects like inelastic deformation, rate of deformation or micro-cracking influence the material's behavior. Since fiber reinforced polymers (FRPs) with aligned fibers can be idealized as UD on a sufficiently small length scale, the majority of constitutive models have been developed for this specifically. Many different approaches to capture the complex deformation behavior have been proposed in the literature, making fundamentally different assumptions on the sources of non-linearity and thus varying greatly in their applicability.

1.2. State of the art

A common approach is to model all non-linear effects using continuum damage mechanics (CDM). This is based on the fundamental idea of replacing microscopic defects with a surrogate continuum with equivalent resulting properties, pioneered individually by Kachanov [12] and Rabotnov [13]. It was adapted to FRP by Ladéveze and LeDantec [14] as well as Talreja [15]. Based on this foundation, Salavatian and Smith took the relationship between matrix crack density and continuous damage variables as basis for their derivation of interaction mechanism between transverse and shear damage, allowing for an accurate assessment of the influence of crack closure on shear behavior [16]. Ge et al. extended the idea of coupling transverse and shear damage to a 3D model and combined this with failure model specific damage evolution to predict the behavior of fiber bundles in braids [17]. To reduce mesh dependency in the case of strain softening, Singh et al. developed an approach to link characteristic element length to material parameters in the Hashin criterion [18] and combined it with different evolution laws [19]. Using a multi-scale model, Park et al. leveraged the inherent dependency of the material parameters on effects at smaller scales to determine parameters for a CDM approach combined with non-linear elastic behavior in the fiber direction, thus reducing experimental effort for parameter identification (PI) [20]. Furtado et al. extended a 2D CDM model by taking the effect of compressive through thickness stress on fiber kinking and the damage evolution under in plane shear into account [21]. This was shown to greatly improve simulation predictions of the filled-hole compression test, where a pre-stressed bolt applies out-of-plane stress to the specimen.

Since CDM cannot capture the permanent deformation FRTs exhibit after unloading, many authors have introduced aspects of plasticity theory. To incorporate the hysteresis effects observed during unloading and reloading of a carbon fiber reinforced polymer (CFRP), Fallahi and Taheri-Behrooz proposed so-called "plastic-elastic" strain that leads to recoverable deformation while dissipating energy [22]. Similarly, Còzar et al. developed a 3D invariant based plasticity model that captures the deformation behavior of CFRP coupon specimens of various off-axis angles and combined it with CDM to predict onset and propagation of damage [23]. They further refined the failure model in terms of damaged, instead of effective, stress to prevent spurious damage in the transverse direction under longitudinal loading [24]. Goncalves et al. picked up the idea of an invariant based plasticity formulation and coupled it with a smeared crack approach to allow for implicit time integration [25]. They extended it to consider interaction of transverse and longitudinal damage [26]. A similar idea was proposed by Hoffarth et al., who first developed an anisotropic plasticity model with a non-associative flow rule [27] which they later extended by a reduced Matzenmiller damage model [28] to simulate low velocity impact events [29]. Building on these ideas, Chen and Li showed that linear evolution laws for damage as well as plasticity can be sufficient when applied mode specific and plasticity is formulated using damage affected stress [30].

Even though many of the works mentioned so far were successfully employed, even in crash and impact simulations, they generally do not account for the strain rate dependency of FRP behavior. Treutenaere et al. addressed this by using a generalized Maxwell model for the fundamental stress decomposition into equilibrium and time dependent parts [31]. By combining this with CDM, they achieved excellent agreement in continuous loading experiments at different loading velocities. To reduce the number of material parameters, Fritsch et al. proposed modeling the rate dependent behavior with a single Maxwell-like branch, substituting the Newtonian dashpot with a hyperbolic Eyring one [32]. This allowed them to accurately capture the stress-strain behavior of glass fiber (GF)/polypropylene (PP) under both quasi-static as well as dynamic test conditions. Gerritzen et al. used a data-driven approach to capture the non-linear out of plane shear behavior of FRTs [33]. By combining it with phenomenological models, strain rate dependency across a wide range could be represented accurately.

In order to obtain models with predictive capabilities under more general loading conditions, further interactions have been included: Chen and Morozov extended a 2D-model taking CDM and plasticity into account by incorporating a strain rate dependent yield criterion [34]. This allowed for the accurate prediction of both static as well as dynamic coupon tests. Similarly, Kerschbaum and Hopmann proposed a plane stress model combining CDM and plasticity with an empirical scaling law for strain rate dependency of stiffness as well as strength values proposed by Wiegand [35,36]. Zhai et al. combined CDM, plasticity and viscoelasticity to accurately model the behavior of glass fiber polypropylene (GF/PP) throughout loading-unloading recovery tests with several off-axis angles [37]. A similar combination of sub-models with the additional hyperbolic viscoelasticity model from Fritsch et al. [32] was proposed by Zscheyge et al. [38]. They combined it with a novel stepwise loading-unloading test with relaxation and retardation periods for efficient PI. Following this, the comprehensive set of 21 parameters can be determined from just a standard characterization program of continuous loading of 0°, 90° and ±45° specimens together with two additional tests. The generalization capabilities of this 2D model have since been shown by Andriß et al., who successfully applied it to a CFRP with polycarbonate matrix [39].

1.3. Outline

The highly generalized material models for composites with thermoplastic matrix systems have been developed for a plane stress state. This significantly limits the applicability of such advanced models, e.g., prohibiting the analysis of manufacturing and mechanical joining processes with their resulting complex material structures like pin pressing or self piercing riveting [40–42]. Therefore, the aim of this work is to extend the model proposed in [38] to a general stress state. Its functionality is extensively tested on coupon level, and validated using three point impact bending (3 P-IB) tests performed on a specialized rig developed in [43,44].

2. Extension of the constitutive model to general stress states

To extend the applicability of the model proposed by Zscheyge et al. [38] to arbitrary stress states and thus allow for its usage in general purpose finite element analysis (FEA), the individual submodels are adapted accordingly. The fundamental idea of modeling the laminate behavior on the level of its individual UD plies, as demonstrated successfully in various other works, see e.g., [45,46], is further pursued. For a single direction, the submodel interactions may be derived from the rheological surrogate shown in Fig. 1.

The application of the experimental methodology developed by Zscheyge et al. [38] allows for a clear distinction of a) time dependent

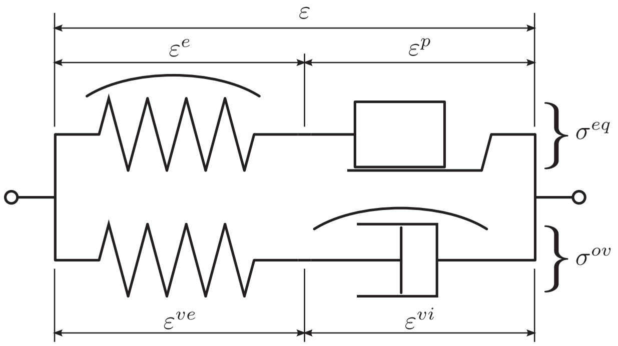

Fig. 1. 1D rheological surrogate for the constitutive model.

and independent effects through extended holding periods and b) of inelastic deformation (modeled as plasticity and represented by the friction element) and changes in stiffness (modeled as damage and represented by the non-linear spring) through unloading. They found no conclusive evidence for the viscoelastic behavior interacting with the damage up to $\dot{\varepsilon} = 1.0e-11/s$, so damage is considered rate independent. The overall relationship of stress $\underline{\sigma}$ and total strain $\underline{\varepsilon}$ can be written as:

$$\underline{\sigma} = \underbrace{\underline{\underline{\tilde{C}}}\left(\underline{\varepsilon} - \underline{\varepsilon}^p\right)}_{=:\underline{\sigma}^{eq}} + \underline{\sigma}^{ov} \quad , \tag{1}$$

with the effective stiffness matrix $\underline{\underline{\tilde{C}}}$, governed by CDM, and plastic strain $\underline{\varepsilon}^p$ affecting equilibrium stress $\underline{\sigma}^{eq}$ and the viscoelastic overstress $\underline{\sigma}^{ov}$.

Modeling assumptions for the GF/PP under investigation: In this study, an FRTs made of a UD non-crimped E-GF fabric and a Borealis BJ100-HP PP [47] matrix, which was used in a variety of recent studies [41,48] are utilized. A more detailed analysis of the material can be found in [49]. To incorporate simplifying experimental observations regarding the deformation behavior of UD plies and to prevent further increasing the already large number of 25 material parameters, the following assumptions and decisions were made throughout the derivation of the 3D constitutive model:

- Each UD ply is assumed to behave transversely isotropic for all modeled aspects of the deformation behavior, with the primary axis denoted by 1 as shown in Fig. 2. Hence, the mapping of coordinates to FRP typical symbols $\parallel \,\hat{=}\, 1$ for the fiber direction and $\perp \,\hat{=}\, 2 \,\hat{=}\, 3$ for the directions perpendicular to the fibers. This leads to the relationships between independent and directional parameters given exemplarily for the elastic properties in Eq. (2).

$$\begin{aligned} E_1 &= E_{\parallel}, & E_2 &= E_3 = E_{\perp} \\ \nu_{23} &= \nu_{\perp\perp}, & \nu_{12} &= \nu_{13} = \nu_{\parallel\perp} \\ G_{23} &= \frac{E_{\perp}}{2\left(1+\nu_{\perp\perp}\right)}, & G_{12} &= G_{13} = G_{\parallel\perp} \end{aligned} \tag{2}$$

- Material behavior in the fiber direction is purely elastic and strain rate independent. In tension this is linear, in compression however some non-linearities occur because of fiber evasion [14,50,51].
- Ductile damage of UD plies has been found to only accumulate under tensile loading perpendicular to the fiber direction and shear loading [52], all other modes lead to immediate total failure. Therefore, only these two modes are considered for damage initiation and evolution.
- For the reference yield strength, values perpendicular to the fiber direction are chosen. Since a linear trend for effective stress and effective plastic strain could be identified in [38] by sequential decomposition into underlying phenomena, the hardening behavior is modeled using a constant tangent modulus T.
- The reference stress for viscoelasticity is modeled as dependent on the strain rate using a power law: $\sigma_0 = a\,\dot{\varepsilon}^b$ with separate parameters a, b under normal and shear loading.
- Due to the pronounced rate dependency of PP it is possible to identify model parameters for strain rate dependency from quasi-static tests ($\dot{\gamma} = 2.2e-41/s$) and extrapolate to elevated strain rates. This is validated for the material under investigation up to a strain rate of $\dot{\gamma} = 2.2e-21/s$. Extrapolation from $\dot{\gamma} = 2.2e-41/s$ to a range of $\dot{\gamma} = 1.e-61/s$ to $\dot{\gamma} = 1.e-11/s$ has previously been shown for a similar GF/PP [38].

It must be noted that the proposed model does not take total failure of the UD plies into account. Therefore, the derived model is suitable to assess strain rate dependent deformation and damage behavior, but not to predict ultimate loads.

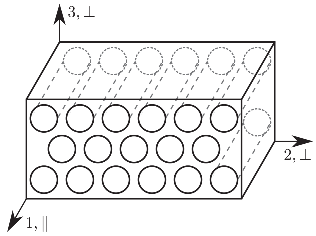

Fig. 2. Alignment of cartesian and fiber coordinate system for an idealized UD ply.

2.1. Equilibrium behavior

Within this section a model for the material's rate independent stress response $\underline{\sigma}^{eq}$ is derived.

2.1.1. Elasticity

The initial stress-strain-relationship in a tension state is considered to be linear. Therefore the generalized Hooke's law is used for its modeling. The aforementioned loss in stiffness in fiber direction under compression is modeled following the proposal by Ladèveze and LeDantec [14] with an effective Young's modulus in fiber direction:

$$\tilde{E}_1 = E_1 \left(1 + \gamma \, \langle \sigma_1 \rangle^{(-)}\right) = E_1 \, \Gamma \quad , \tag{3}$$

introducing the material parameter for fiber evasion γ and the resulting stiffness loss factor Γ. Insertion of the effective Young's modulus into the compliance matrix $\underline{\underline{S}}$ leads to an asymmetric matrix. However, from the symmetry requirements $S_{1i} = S_{i1}$; $\nu_{1i}/\tilde{E}_1 = \nu_{i1}/E_i = \text{const.}$ follows.[1] To satisfy this in the case stiffness reduction ($\Gamma < 1$), reduced Poisson's ratios in the compressive state are defined:

$$\tilde{\nu}_{1i} = \nu_{1i}\,\Gamma; \quad i = 2, 3. \tag{4}$$

The stiffness matrix $\underline{\underline{C}}$ is obtained by inverting $\underline{\underline{S}}$. When using an EULER-forward time integration scheme for uniaxial fiber parallel compression, the implementation of Γ according to (3) led to time step dependent oscillations in the stress response. In order to prevent these, a mathematically equivalent formulation was linearized, stabilizing the simulations. Details on the adaptation are given in Appendix A.

2.1.2. Damage modeling

The permanent decrease in stiffness due to defect initiation and growth is modeled using CDM. Following the proposal by Matzenmiller et al. [28], a damage matrix $\underline{\underline{D}}$ is introduced:

$$\underline{\underline{D}} = \operatorname{diag}\left(1, \frac{1}{1-d_{22}}, \frac{1}{1-d_{33}}, \frac{1}{1-d_{23}}, \frac{1}{1-d_{13}}, \frac{1}{1-d_{12}}\right), \tag{5}$$

with the damage variables d_{ij}. Here, no damage is considered in the fiber direction, from which $d_{11} \equiv 0$ and thus $D_{11} \equiv 1$ follow. With $\underline{\underline{D}}$, the

---

[1] At Poisson's ratios ν_{ij} i denotes the primary loading direction and j the direction of resulting transverse strain.

effective stress $\underline{\tilde{\sigma}}$, representing the stress in a virtual undamaged material with reduced cross section and effective strain $\underline{\tilde{\varepsilon}}$, representing the strain in such a virtual material, are defined:

$$\begin{aligned} \underline{\tilde{\sigma}} &= \underline{\underline{D}}\,\underline{\sigma} \quad \text{and} \\ \underline{\tilde{\varepsilon}} &= \underline{\underline{D}}^{-1}\,\underline{\varepsilon}. \end{aligned} \tag{6}$$

This leads to a preliminary effective compliance matrix:

$$\underline{\underline{\tilde{S}}}_{\text{prelim}} = \underline{\underline{S}}\,\underline{\underline{D}}^{-1} \quad . \tag{7}$$

Given the observations of Kashtalyan and Soutis [53] that Poisson's ratios are effected by the damage state as well, further effective Poisson's ratios are defined by adding degradation functions as proposed by Ref. [28,52]:

$$\tilde{\nu}_{ij} = \nu_{ij}\left(1 - d_{ii}\right); \quad i \neq j. \tag{8}$$

This ensures symmetry and leads to $\underline{\underline{\tilde{S}}}$. The effective stiffness is obtained by inverting $\underline{\underline{\tilde{S}}}$:

$$\underline{\underline{\tilde{C}}} = \underline{\underline{\tilde{S}}}^{-1} \quad . \tag{9}$$

To determine the onset of damage, an invariant based criterion originally introduced as failure criterion by Cuntze and Freund [54] and adapted by Böhm et al. [52] is used. Invariants regarding rotation around the fiber direction identified in [18] are used as model basis. The used invariants are:

$$\begin{aligned} I_1 &= \tilde{\sigma}_1, & I_2 &= \tilde{\sigma}_2 + \tilde{\sigma}_3, \\ I_3 &= \tilde{\tau}_{12}^2 + \tilde{\tau}_{13}^2 \quad \text{and} & I_4 &= \left(\tilde{\sigma}_2 - \tilde{\sigma}_3\right)^2 + 4\tilde{\tau}_{23}^2. \end{aligned} \tag{10}$$

Furthermore, Cuntze proposes five basic failure modes for UD-plies and individual criteria to accurately describe failure in each of them [54–56]. These five criteria are then combined through a probabilistic coefficient to obtain one overall criterion.

The respective criteria can be written as:

$$\begin{aligned} H_{\parallel}^{(+)} &= \frac{I_1}{R_{\parallel}^{(+)}} - r_{\parallel}^{(+)} = 0, & H_{\parallel}^{(-)} &= \frac{-I_1}{R_{\parallel}^{(-)}} - r_{\parallel}^{(-)} = 0, \\ H_{\perp}^{(+)} &= \frac{I_2 + \sqrt{I_4}}{2R_{\perp}^{(+)}} - r_{\perp}^{(+)} = 0, & H_{\perp}^{(-)} &= \frac{\left(b_{\perp\perp}^{C} - 1\right)I_2 + b_{\perp\perp}^{C}\sqrt{I_4}}{R_{\perp}^{(-)}} - r_{\perp}^{(-)} = 0 \text{ and} \\ H_{\parallel\perp} &= \frac{\sqrt{I_3} + b_{\parallel\perp}^{C} I_2}{R_{\parallel\perp}} - r_{\parallel\perp} = 0, \end{aligned} \tag{11}$$

with the material parameters $b_{\parallel\perp}^{C}$ and $b_{\perp\perp}^{C}$ describing internal friction and the respective initial strengths R_j [52]. The resulting criterion is then defined using the interaction coefficient $\dot{m}$ [54,55]:

$$H = \left[\sum_j \left(H_j\right)^{\dot{m}}\right]^{\frac{1}{\dot{m}}} - r = 0; \quad j = \parallel, \perp, \parallel\perp \quad . \tag{12}$$

Once damage has been initiated, its evolution is determined individually for each of the failure modes. For this, the mode specific efforts r_j are determined from (11). Based on those efforts, mode specific damage is determined by:

$$\phi_j = \begin{cases} 0 & \text{for } r < 1 \\ \tanh\left[\beta_j\left(r_j - r_{j0}\right)^{\kappa_j}\right] & \text{for } r \geq 1 \end{cases} , \tag{13}$$

with the material parameters β_j and κ_j and the damage threshold r_{j0} which takes the value of r_j when $r = 1$ is first satisfied [52]. The damage variables in the fiber coordinate system are determined by:

$$d_i^{\dot{m}} = \sum_j \left(\phi_j q_i^j\right)^{\dot{m}}, \tag{14}$$

where mode interaction is taken into account by the coefficients q_i^j [52,57]. Since experimental results show immediate total failure if damage occurs in one of the modes described by $H_{\parallel}^{(+)}$, $H_{\parallel}^{(-)}$or $H_{\perp}^{(-)}$, these are not considered in damage evolution but would trigger an instant failure criterion [52]. Hence, $\underline{\underline{D}}$ can be expressed in terms of mode specific damage variables using

$$d_{22} = d_{33} = d_{23} = d_{\perp} \quad \text{and} \quad d_{12} = d_{13} = d_{\parallel\perp} \quad , \tag{15}$$

with $d_{\perp}$ acting on the behavior in the plane of isotropy and $d_{\parallel\perp}$ affecting the shear behavior with one axis parallel to the fiber direction.

2.1.3. *Plasticity formulation and interaction with damage*

Inelastic deformation is taken into account by a plasticity model. A yield criterion based on the proposal by Hill [58] in combination with isotropic hardening and associated flow is used. As proposed by Ref. [14], interaction between plasticity and damage is considered by usage of effective stress in the yield criterion and thus the flow rule. An effective equivalent stress is defined as:

$$\tilde{\sigma}_e = \sqrt{\left(\underline{\underline{D}}\,\underline{\sigma}\right)^T \underline{\underline{A}}\,\underline{\underline{D}}\,\underline{\sigma}}, \tag{16}$$

with the coefficient matrix $\underline{\underline{A}}$:

$$\begin{aligned} \underline{\underline{A}} &= \frac{1}{F+G+H}\begin{bmatrix} \underline{\underline{A}}_1 & \underline{\underline{0}} \\ \underline{\underline{0}} & \underline{\underline{A}}_4 \end{bmatrix} \\ \underline{\underline{A}}_1 &= \begin{bmatrix} G+H & -H & -G \\ -H & H+F & -F \\ -G & -F & F+G \end{bmatrix}, \quad \underline{\underline{A}}_4 = 2\,\mathrm{diag}(L, M, N). \end{aligned} \tag{17}$$

The parameters F, G, H, L, M, N can be written in terms of the initial yield stresses Y_{ij} as:

$$\begin{aligned} F &= \frac{1}{2}\left(\frac{1}{Y_{22}^2} + \frac{1}{Y_{33}^2} - \frac{1}{Y_{11}^2}\right) & L &= \frac{1}{2\,Y_{23}^2} \\ G &= \frac{1}{2}\left(\frac{1}{Y_{22}^2} + \frac{1}{Y_{11}^2} - \frac{1}{Y_{33}^2}\right) & M &= \frac{1}{2\,Y_{13}^2} \\ H &= \frac{1}{2}\left(\frac{1}{Y_{11}^2} + \frac{1}{Y_{33}^2} - \frac{1}{Y_{22}^2}\right) & N &= \frac{1}{2\,Y_{12}^2}. \end{aligned} \tag{18}$$

Using this,

$$f = \tilde{\sigma}_e - Y = 0 \tag{19}$$

with the reference yield stress Y follows for the final yield criterion. Thereupon, plastic strain rate is defined by:

$$\underline{\dot{\varepsilon}}^p = \dot{\lambda}\,\frac{\partial f}{\partial \underline{\sigma}}, \tag{20}$$

with the consistency factor $\dot{\lambda}$ which has to be determined. Furthermore an effective plastic strain rate is defined by:

$$\underline{\dot{\tilde{\varepsilon}}}^p = \dot{\lambda}\,\frac{\partial f}{\partial \underline{\tilde{\sigma}}} = \underline{\underline{D}}^{-1}\,\underline{\dot{\varepsilon}}^p. \tag{21}$$

Using (21) a rate of effective equivalent plastic strain $\dot{\tilde{\varepsilon}}_e^p$ can be defined, for which

$$\dot{W}^p = \underline{\sigma}^T\,\underline{\dot{\varepsilon}}^p = \underline{\underline{D}}\,\underline{\sigma}^T\,\underline{\underline{D}}^{-1}\,\underline{\dot{\varepsilon}}^p = \underline{\tilde{\sigma}}^T\,\underline{\dot{\tilde{\varepsilon}}}^p = \tilde{\sigma}_e \dot{\tilde{\varepsilon}}_e^p \tag{22}$$

with the rate of plastic work $\dot{W}^p$ as shown in [59]. It is shown in Appendix B that for the chosen yield criterion in combination with an associative flow rule $\dot{\lambda} = \dot{\tilde{\varepsilon}}_e^p$ follows.

This leads to

$$\dot{\tilde{\varepsilon}}_e^p = \sqrt{\left(\dot{\tilde{\underline{\varepsilon}}}^p\right)^T \underline{\underline{a}}\,\dot{\tilde{\underline{\varepsilon}}}^p} \quad , \tag{23}$$

with

$$\underline{\underline{a}} = (F+G+H)\begin{bmatrix} \underline{\underline{a}}_1 & \underline{\underline{0}} \\ \underline{\underline{0}} & \underline{\underline{a}}_4 \end{bmatrix} \tag{24}$$

and

$$\underline{\underline{a}}_1 = \frac{1}{(F\,G+F\,H+G\,H)^2}\begin{bmatrix} F^2\,(G+H) & -2\,F\,G\,H & -2\,F\,G\,H \\ -2\,F\,G\,H & G^2\,(F+H) & -2\,F\,G\,H \\ -2\,F\,G\,H & -2\,F\,G\,H & H^2\,(F+G) \end{bmatrix},$$

$$\underline{\underline{a}}_4 = \operatorname{diag}\left(\frac{1}{2\,L},\frac{1}{2\,M},\frac{1}{2\,N}\right) \quad .$$

From this, the effective equivalent plastic strain is defined as:

$$\tilde{\varepsilon}_e^p = \int_{-\infty}^{t} \dot{\tilde{\varepsilon}}_e^p\,\mathrm{d}t \quad . \tag{25}$$

Based on $\tilde{\varepsilon}_e^p$ isotropic hardening is defined by

$$Y = Y\left(\tilde{\varepsilon}_e^p\right) \quad . \tag{26}$$

The consistency factor $\dot{\lambda}$ can be determined by evaluating the consistency condition [60]:

$$f + \dot{f} = 0 \quad , \tag{27}$$

which leads to

$$\dot{f} = \left(\frac{\partial f}{\partial \underline{\sigma}}\right)^T \dot{\underline{\sigma}} + \frac{\partial f}{\partial \tilde{\varepsilon}_e^p}\dot{\tilde{\varepsilon}}_e^p + \mathrm{Tr}\left(\frac{\partial f}{\partial \underline{\underline{D}}}\dot{\underline{\underline{D}}}\right) = 0 \tag{28}$$

when yielding. Here, derivatives with respect to a vector or matrix are defined elementwise by

$$\frac{\partial f}{\partial \underline{\sigma}} = \left[\frac{\partial f}{\partial \sigma_1},\frac{\partial f}{\partial \sigma_2},\dots,\frac{\partial f}{\partial \sigma_i}\right]^T \tag{29}$$

$$\frac{\partial f}{\partial \underline{\underline{D}}} = \begin{bmatrix} \frac{\partial f}{\partial D_{11}} & \frac{\partial f}{\partial D_{12}} & \cdots & \frac{\partial f}{\partial D_{1j}} \\ \vdots & \ddots & & \vdots \\ \frac{\partial f}{\partial D_{i1}} & \frac{\partial f}{\partial D_{i2}} & \cdots & \frac{\partial f}{\partial D_{ij}} \end{bmatrix} \quad . \tag{30}$$

In (28) $\dot{\tilde{\varepsilon}}_e^p$ is substituted by the consistency factor $\dot{\lambda}$ and $\dot{\underline{\sigma}}$ is substituted by Hooke's law, taking into account the change in deformation state ($\dot{\underline{\varepsilon}}^e$) as well as in stiffness ($\dot{\tilde{\underline{\underline{C}}}}$):

$$\dot{\underline{\sigma}} = \tilde{\underline{\underline{C}}}\,\dot{\underline{\varepsilon}}^e + \dot{\tilde{\underline{\underline{C}}}}\,\underline{\varepsilon}^e = \tilde{\underline{\underline{C}}}\,\left(\dot{\underline{\varepsilon}} - \dot{\underline{\varepsilon}}^p\right) + \dot{\tilde{\underline{\underline{C}}}}\,\underline{\varepsilon}^e = \tilde{\underline{\underline{C}}}\,\left(\dot{\underline{\varepsilon}} - \dot{\lambda}\frac{\partial f}{\partial \underline{\sigma}}\right) + \dot{\tilde{\underline{\underline{C}}}}\,\underline{\varepsilon}^e \quad . \tag{31}$$

Using nominal stress increments in (28) has the advantage of being associated with the effective stiffness $\tilde{\underline{\underline{C}}}$ and thus allows to take the degradation of Poisson's ratios into account. Solving (28) for $\dot{\lambda}$ finally leads to

$$\dot{\lambda} = \frac{\left(\frac{\partial f}{\partial \underline{\sigma}}\right)^T \tilde{\underline{\underline{C}}}\,\dot{\underline{\varepsilon}} + \left(\frac{\partial f}{\partial \underline{\sigma}}\right)^T \dot{\tilde{\underline{\underline{C}}}}\,\underline{\varepsilon}^e + \mathrm{Tr}\left(\frac{\partial f}{\partial \underline{\underline{D}}}\dot{\underline{\underline{D}}}\right)}{\left(\frac{\partial f}{\partial \underline{\sigma}}\right)^T \tilde{\underline{\underline{C}}}\left(\frac{\partial f}{\partial \underline{\sigma}}\right) - \frac{\partial f}{\partial \tilde{\varepsilon}_e^p}} \quad , \tag{32}$$

with

$$\frac{\partial f}{\partial \underline{\sigma}} = \frac{\underline{\underline{D}}\,\underline{\underline{A}}\,\underline{\underline{D}}\,\underline{\sigma}}{\tilde{\sigma}_e} \quad \text{and} \tag{33}$$

$$\frac{\partial f}{\partial \underline{\underline{D}}} = \frac{\underline{\underline{A}}\,\underline{\underline{D}}\,\underline{\sigma}\,\underline{\sigma}^T}{\tilde{\sigma}_e} \quad . \tag{34}$$

Final formulae for UD material. Applying the presented assumptions leads to the simplification of Eq. (16):

$$\tilde{\sigma}_e = \sqrt{\left(\tilde{\sigma}_2 - \tilde{\sigma}_3\right)^2 + \left(\frac{R_2\,\tilde{\tau}_{23}}{R_{23}}\right)^2 + \left(\frac{R_2}{R_{12}}\right)^2\left(\tilde{\tau}_{13}^2 + \tilde{\tau}_{12}^2\right)} \quad . \tag{35}$$

In case of the rate of effective equivalent plastic strain, the fact that both factors G and H go to 0 as a result of the assumptions, prevents the formal derivation from Eq. (23). It is instead derived in Appendix C, leading to

$$\dot{\tilde{\varepsilon}}_e^p = \sqrt{\left(\frac{\dot{\tilde{\varepsilon}}_2^p - \dot{\tilde{\varepsilon}}_3^p}{2}\right)^2 + \left(\frac{R_{23}}{R_2}\right)^2\left(\dot{\tilde{\gamma}}_{23}^p\right)^2 + \left(\frac{R_{12}}{R_2}\right)^2\left(\left(\dot{\tilde{\gamma}}_{13}^p\right)^2 + \left(\dot{\tilde{\gamma}}_{12}^p\right)^2\right)} \quad . \tag{36}$$

2.2. Strain rate dependency

The dependency of the material behavior on the loading velocity is modeled as strain rate dependency. For its description a rheological approach is taken, using a Maxwell-Element with a non-linear Eyring damper as shown in Fig. 1

For the damper

$$\sigma^{ov} = \sigma_0\,\mathrm{arcsinh}\left(\frac{\dot{\varepsilon}}{\dot{\varepsilon}_0}\right) \tag{37}$$

with a reference stress σ_0 and reference strain rate $\dot{\varepsilon}_0$ is assumed. This leads to

$$\dot{\sigma}^{ov} = E_r\dot{\varepsilon} - E_r\dot{\varepsilon}_0\sinh\frac{\sigma^{ov}}{\sigma_0} = E_r\dot{\varepsilon} - \frac{\sigma_0}{\tau_r}\sinh\frac{\sigma^{ov}}{\sigma_0} \tag{38}$$

for the entire Maxwell-Element [32], with the spring's stiffness E_r and the relaxation time $\tau_r = \sigma_0/(E_r\,\dot{\varepsilon}_0)$.

The generalization of this behavior is carried out under the assumption that only the associated strain's rate has an effect on the stress, e.g., σ_{22}^{ov} is solely dependent on $\dot{\varepsilon}_{22}$. This assumption is made to avoid the introduction of new material parameters and significantly expanding the experimental effort. Therefore, Eq. (38) is applied to each over-stress component individually, excluding the fiber direction.

3. Experimental methods and results

3.1. Conducted experiments for parameter identification and validation

The applicability of the developed extension of the constitutive model is investigated in a staggered approach: First, the overall stress-strain behavior is assessed and ultimate strength values of an FRTs are determined. For 0°- and 90°-direction, specimens in accordance with DIN EN ISO 527–5 [61], and for in-plane shear properties [±45°] specimens in accordance with DIN EN ISO 14,129 [62] were used. Additionally, the material's specific relaxation time was determined by deforming a specimen with $[45^\circ_2/-45^\circ_2]_\mathrm{s}$ layup to a longitudinal strain of 1.4 % at a loading velocity of $1\ ^{\mathrm{mm}}/_{\mathrm{min}}$ and subsequently holding for 56 h allowing the stress response to reach a stationary state. Since the necessary time would make subsequent stepwise tests infeasibly long, a time of 5 h, corresponding to 85 % stress decay, is chosen as holding time in subsequent tests. The final equilibrium response is obtained post hoc by extrapolation to 100 % stress decay. Next, the experimental methodology with stepwise loading-unloading tests with relaxation and retardation periods proposed in [38] is applied to $[90^\circ]_8$ and $[45^\circ_2/-45^\circ_2]_\mathrm{s}$ specimens to determine the material parameters. Each cycle begins with a strain controlled loading up to a target strain, followed by a relaxation period. Subsequently, the specimen is unloaded until a longitudinal force of 0 N is reached. Each cycle is concluded with a force controlled retardation period, remaining at 0 N. Strain levels of for the holding periods are based on the stress-strain results from the standardized tests. For validation of the PI, standardized tests are repeated at $16^{\mathrm{mm}}/_{\mathrm{min}}$ and specimens with $[30^\circ{}_2/{-60}^\circ{}_2]_\mathrm{s}$ layup are tested both under continuous as well as stepwise loading conditions. Finally, 3 P-IB experiments with a span of 30 mm and impact velocity ranging from $4.5\ ^{\mathrm{m}}/_{\mathrm{s}}$ to $9.0\ ^{\mathrm{m}}/_{\mathrm{s}}$ are carried out on a 3 P-IB rig, originally developed in [63], including the refinements from Ref. [43,44]. It is shown in Fig. 3.

The set-up uses a titanium bar of 9.81 mm diameter and 500 mm length with a tip radius of 3 mm as impactor. It is instrumented with a

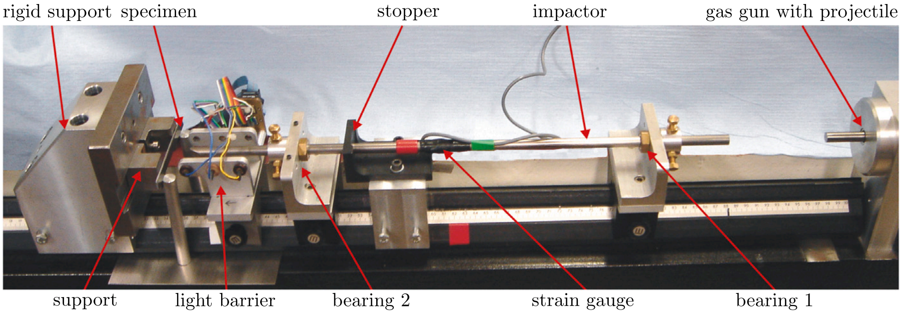

Fig. 3. Test set-up used for three point impact bending (3P-IB).

Table 1
Specification of the utilized specimens.

Intention	Loading	Velocity	Dimension	Layup	Ref.
Fundamental behavior	Continuous	$1^{\mathrm{mm}}/_{\mathrm{min}}$	15×250 x 1mm^3	$[0°]_4$	[61]
			25×250 x 2mm^3	$[90°]_8$	
				$[45°_2/-45°_2]_s$	[62]
Relaxation time	Relaxation	$1^{\mathrm{mm}}/_{\mathrm{min}}$	25×250 x 2mm^3	$[45°_2/-45°_2]_s$	[62]*
PI	Stepwise	$1^{\mathrm{mm}}/_{\mathrm{min}}$	25×250 x 2mm^3	$[90°]_8$	[38]*
				$[45°_2/-45°_2]_s$	
Validation	Continuous	$16^{\mathrm{mm}}/_{\mathrm{min}}$	25×250 x 2mm^3	$[90°]_8$	[61]
				$[45°_2/-45°_2]_s$	[62]
				$[30°_2/-60°_2]_s$	[61]*
		$100^{\mathrm{mm}}/_{\mathrm{min}}$	25×250 x 2mm^3	$[45°_2/-45°_2]_s$	[62]
	Stepwise	$2^{\mathrm{mm}}/_{\mathrm{min}}$	25×250 x 2mm^3	$[30°_2/-60°_2]_s$	[38]*
	Impact	4.5…9.0 $^{\mathrm{m}}/_{\mathrm{s}}$	9×90 x 3mm^3	$[(0°/90°)_3]_s$	[43,44]*

*adapted from reference

strain gauge, measuring strain waves resulting from the impact. Based on the Hopkinson bar principle, i.e. using the strain waves in the bar to obtain information on events at the impact location, acting force at the impactor tip can be calculated. The contact region of the steel supports is manufactured with a 3 mm radius as well. Due to restricted availability of the material, the specimens for 3 P-IB tests were made from the GF/PP used in [38]. An overview of all conducted tests, the respective lay-up, geometry and loading conditions is given in Table 1. All continuous load test cases are carried out with a standard testing machine Zwick Z2,5 (ZwickRoell GmbH & Co KG), whereas the stepwise loading cases are performed on a servohydraulic testing machine Schenck Hydropulser PC63M-50.

3.2. *Experimental results*

3.2.1. *Quasi-static continuous tensile tests*

The fundamental direction-dependent material behavior is identified by tensile tests. Parallel to the fiber direction, the UD material exhibits linear behavior up to final failure. The corresponding stress-strain-curve is shown in Appendix D: Fig. D.20. For transverse tension and shear resulting stress-strain-curves are shown in Fig. 4.[2]

For the 90 °-specimens the tensile stress increases up to a strain $\varepsilon_2 \approx 0.005$, it remains almost constant at 15 MPa with increasing strain (Fig. 4a). The respective failure strains $\varepsilon^{\mathrm{fail}}$ vary significantly between 0.041 and 0.081. Hence, the first strain level for the stepwise loading is defined in the elastic region below the maximum strength at $\varepsilon_2 = 2.5e-3$. The second step is chosen to closely match the transition from stress increase to stress plateau. Additionally, two strain levels are chosen with sufficient distance from the lowest failure strain $\varepsilon^{\mathrm{fail}} = 0.041$. The chosen strain levels are summarized in Table 2 and indicated in the figure by dashed vertical lines (Fig. 4a).

The stress-strain-curves of the ±45 °-specimens exhibit a sublinear growth profile without a distinctive plateau (Fig. 4b). Failure is initiated uniformly upon reaching a stress of 19.4 MPa. Therefore, the strains for the load steps are distributed up to a limit of 0.026, with increasing distance. This limit strain corresponds to the shear stress τ_{12} of 16 MPa, which is approximately 85 % of the maximum shear stress. This is done to prevent specimen failure during the stepwise loading and unloading test. Chosen strain levels for PI are given in Table 2 and indicated in Fig. 4b.

Since pronounced non-linearity occurs in the strain regime in which Young's moduli are determined for transverse and shear behavior, these values are not used further. Only Poisson ratios and Young's modulus in fiber direction obtained from these experiments are used for the further work. They are presented alongside elastic moduli determined according to standards indicated in Table 1 for all directions as well as the material strength values in Table 3.

3.2.2. *Relaxation experiments*

Necessary holding time to obtain a stationary state is determined by loading a $[45°_2/-45°_2]_s$ specimen to $\gamma = 1.4\,\%$ at $1^{\mathrm{mm}}/_{\mathrm{min}}$ and subsequent strain controlled holding for 56 h. As shown on the left in Fig. 5, the stress begins to decay as soon as the loading stops at 35 s. Since the stress relaxation is driven by remaining viscoelastic overstress, it decelerates with the advancement of relaxation. However, the stress continues to decrease for 45 h.

Since the specimen has to be held twice per cycle, this implies a duration of 450 h(= 18.75 d) per test. To prevent this infeasible test time, a holding time of 5 h is defined, corresponding to an 85 % decay of

---

[2] Here and in all following figures, specimens are denoted according to the naming scheme defined in the collaborative research center TRR285: A03_F_0_XXX encoding specimen number **XXX** from subproject **A03** made from **F**iber reinforced polymer with**O**ut any joint.

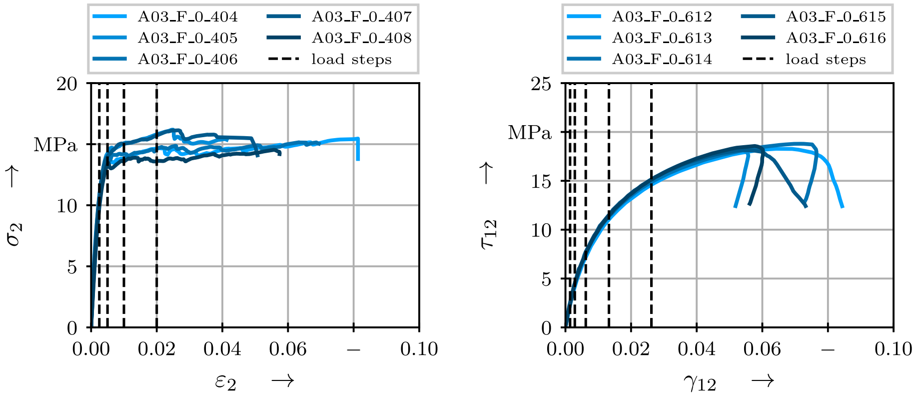

(a) Transverse Tension at $\dot{\varepsilon} = 1.1\text{e}{-4}\,1/\text{s}$

(b) In-plane shear at $\dot{\gamma} = 2.2\text{e}{-4}\,1/\text{s}$

Fig. 4. Experimental results from tests with continuous loading at $v = 1^{\text{mm}}/_{\text{min}}$.

Table 2
Steps for the stepwise loading and unloading tests.

		Cycle 1	Cycle 2	Cycle 3	Cycle 4	Cycle 5
Transverse	ε_2	2.5e-3	5e-3	1e-2	2e-2	
Shear	γ_{12}	1.42e-3	2.86e-3	6.2e-3	1.326e-2	2.62e-2

overstress, from which the total decay is extrapolated in the PI. This allows for a reduced test time of 50 h.

3.2.3. *Stepwise loading and unloading tests for PI*

Based on the quasi-static tensile test the strain and shear strain values for each load cycle are determined and given in Table 2. Given the immense time-wise effort per experiment, only one specimen is tested per configuration, except for the $[90°]_8$ layup, for which three specimens are used to address the more pronounced scattering observed in the preliminary tests. By taking this information into account, two weeks of continuous test time could be saved.

The resulting stress-strain-curves of the $[90°]_8$ samples are presented in Fig. 6a. For each experiment, the envelope of the loading steps behaves very similarly to the continuous tests, including the pronounced plateaus. During the subsequent relaxation periods, a significant decrease in the stress level can be observed. After unloading and retardation, a distinct inelastic strain remains, which increases throughout the cycles. Additionally, the stress-slope of the subsequent loading step is less steep than in the step before. The specimen with a $[45^\circ_2/-45^\circ_2]_s$ layup exhibits similar behavior except for the plateau, as can be seen in Fig. 6b.

From these results, governing parameters are extracted following the methodology developed in [38]. Here, it is described briefly, more details are given in the original work. The total stress value at the end of a loading step $\sigma|_{t=0\ s}$ is taken as reference. From this, the change in stress $\Delta\sigma$ is analyzed for the entire span of 5 h. The measured stress at the end of the relaxation period $\sigma|_{t=18000\ s}$ is extrapolated to the equilibrium stress σ^{eq}, taking into account the remaining 15 % stress relaxation that would have occurred in additional 40 h. This allows for the calculation of the initial viscoelastic overstress $\sigma^{ov}|_{t=0\ s} = \sigma|_{t=0\ s} - \sigma^{eq}$. Based on this, a non-linear curve fit of Eq. (38) is carried out using the `least_squares` algorithm implemented in [64] to identify the material parameters for the strain rate dependent submodel.

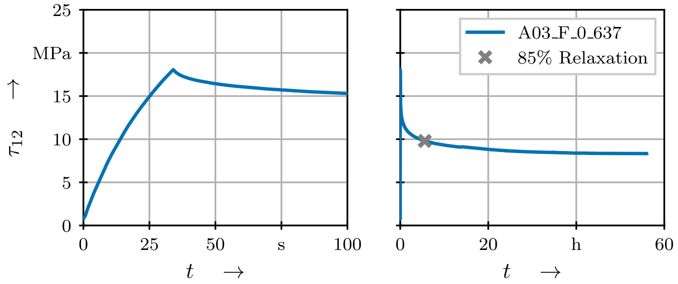

Fig. 5. Stress relaxation in $[45^\circ_2/-45^\circ_2]_s$ specimen at $\gamma = 1.4\,\%$. Left: detailed view at beginning of experiment; Right: entire experiment.

For the equilibrium behavior, strain at the end of loading (ε^{load}) as well as after unloading and retardation (ε^{unload}) is captured. As with the stress, inelastic strain after full retardation (ε^{p}) is obtained by extrapolation from the difference $\Delta\varepsilon = \varepsilon_{load} - \varepsilon_{unload}$. The difference is considered purely elastic, and current modulus is determined by $\tilde{E} = \sigma^{eq}/\Delta\varepsilon$ and in turn current damage $d = 1 - \tilde{E}/E$. This is repeated for each cycle and data correlating effective stress with damage is collected and fitted for Eq. (13), as well as effective plastic strain and hardening for Eq. (26) with constant tangent modulus T. The identified material parameters are given in Table 4.

3.2.4. *Coupon level validation experiments*

As basis for validating the rate dependency, tensile tests with a loading velocity of $16^{\text{mm}}/_{\text{min}}$ and $100^{\text{mm}}/_{\text{min}}$ are conducted. These exhibit a similar behavior to the ones at $1^{\text{mm}}/_{\text{min}}$, but reach a slightly higher stress level on average, as shown in Figs. 7 and 8.

Table 3
Elastic parameters for GF/PP under consideration, determined according to relevant standards.

Elastic	E_1 [MPa]	$E_2 = E_3$ [MPa]	$G_{12} = G_{13}$ [MPa]	ν_{12} [−]	ν_{23} [−]
	31,800 ± (826)	3830 ± (133)	1190 ± (28)	0.24 ± (0.045)	0.38 ± (0.026)*
Strength	R_1 [MPa]	$R_2 = R_3$ [MPa]	$R_{12} = R_{13}$ [MPa]		
	644 ± (22)	15.6 ± (0.7)	19.4 ± (0.3)		

* Lacking experimental results, Poisson ratio of pure matrix is assumed.

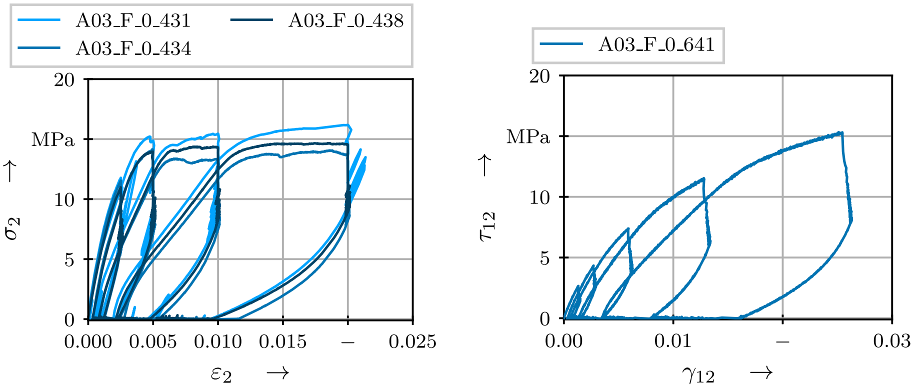

(a) Transverse Tension ($\dot{\varepsilon} = 1.2\mathrm{e}{-4}\,1/\mathrm{s}$)

(b) In-plane shear ($\dot{\gamma} = 2.0\mathrm{e}{-4}\,1/\mathrm{s}$)

Fig. 6. Experimental results from tests with stepwise loading and unloading with relaxation and retardation periods.

Table 4
Material parameters for the investigated GF/PP.

Elasticity		Plasticity		Damage		viscoelasticity	
$E_{\parallel}$	31,800 MPa	$Y_{\perp}$	2.433 MPa	$R_{\perp}$	2.433 MPa	E_r	1928 MPa
$E_{\perp}$	6524 MPa	$Y_{\parallel\perp}$	1.345 MPa	$R_{\perp\parallel}$	1,345 MPa	G_r	918 MPa
$G_{\parallel\perp}$	2300 MPa	T	159,345 MPa	$\kappa_{\perp}$	0.3834	τ_r	20,000 s
$\nu_{\parallel\perp}$	0.24			$\beta_{\perp}$	0.3964	$a_{\parallel}$	0.7035
$\nu_{\perp\perp}$	0.38			$\kappa_{\perp\parallel}$	0.2250	$b_{\parallel}$	0.
γ	0.0005			$\beta_{\perp\parallel}$	0.5300	$a_{\parallel\perp}$	5.4054
				$\dot{m}$	2.5	$b_{\parallel\perp}$	0.5439
				$q_{\perp}^{\perp\parallel}$	0.5		
				$q_{\perp\parallel}^{\perp}$	0.5		

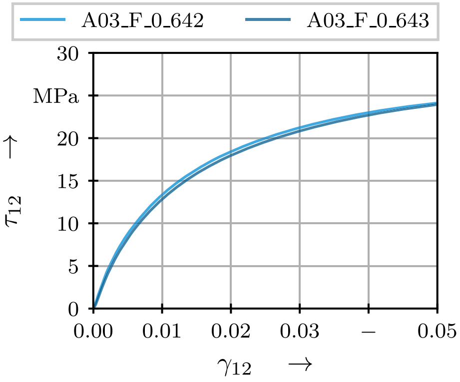

Fig. 8. Experimental results from in-plane shear tests with continuous loading at $v = 100^{\mathrm{mm}}/_{\mathrm{min}}$ ($\dot{\gamma} = 2.2e - 2\,1/\mathrm{s}$).

To further validate the in-plane behavior, tensile tests at $1^{\mathrm{mm}}/_{\mathrm{min}}$ using $[30°_2/{-60°_2}]_s$ specimens were conducted. Similar to the shear dominated tests with $[45^{\circ}_2/-45^{\circ}_2]_s$ layup, the force-displacement behavior exhibits a pronounced non-linearity with sublinear characteristic, as depicted in Fig. 9a. All tested samples show very similar responses and only differ significantly in failure strain.

Additionally, the stepwise-loading and unloading experiment at $2^{\mathrm{mm}}/_{\mathrm{min}}$ with $[30°_2/{-60°_2}]_s$ specimen is used to validate that the differentiation of non-linear effects under a stress combination not used for PI can be accurately predicted. Its force-displacement curve exhibits a beginning similar to the continuously loaded ones with non-linear characteristics, followed by pronounced stress relaxation as well as strain retardation after unloading (Fig. 9b). Evolution of inelastic strain and damage could not be observed, because the specimen failed prematurely during the second relaxation period.

3.2.5. Three point impact bending experiments

The material behavior of the GF/PP during low velocity impact is shown in Fig. 10 for 4.5 and 6.0 $^{\mathrm{m}}/_{\mathrm{s}}$. At an impact velocity of 9 $^{\mathrm{m}}/_{\mathrm{s}}$, the impactor broke the specimen and bounced off the holding aperture. Hence, the results may only be used up to the point of the impactor

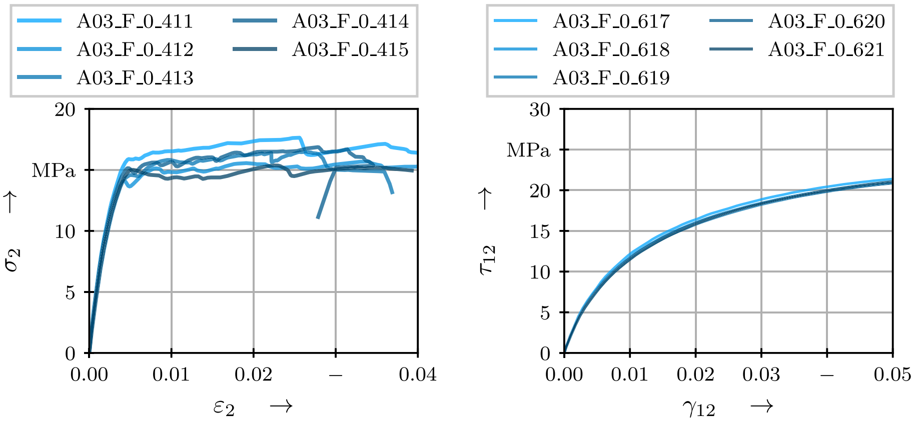

(a) Transverse Tension at $\dot{\varepsilon} = 2.2\mathrm{e}{-3}\,1/\mathrm{s}$

(b) In-plane shear at $\dot{\gamma} = 3.6\mathrm{e}{-3}\,1/\mathrm{s}$

Fig. 7. Experimental results from tests with continuous loading at $v = 16^{\mathrm{mm}}/_{\mathrm{min}}$.

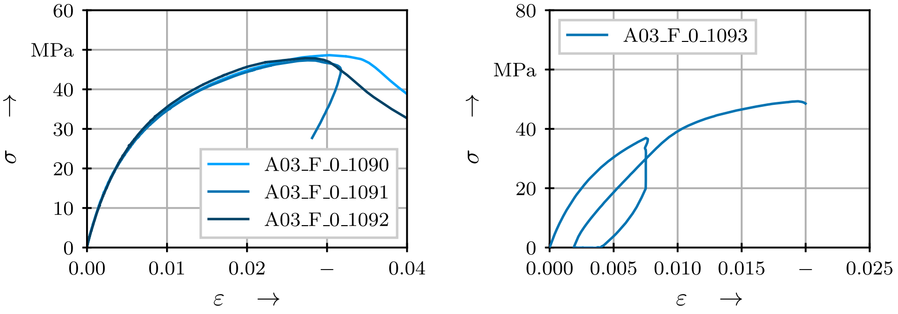

(a) Continuous loading at $\dot{\varepsilon} = 1.3\text{e}{-4}\,1/\text{s}$

(b) Stepwise loading and unloading with relaxation and retardation periods; loading at $\dot{\varepsilon} = 2.6\text{e}{-4}\,1/\text{s}$

Fig. 9. Experimental results from validation tests with $[30°/{-60°}]_s$ layup.

hitting the aperture. They are shown in Appendix E. Since the raw measurement data exhibit pronounced noise, Savitzky–Golay filter with a window size of 101 and polynomial degree of 3 is used to smooth them. Raw measurements are shown with thin lighter lines, analyses are based on the filtered curves. At both velocities, an initial spike in the force signal may be observed, corresponding to the first contact of impactor and specimen. With increasing deflection, the force continues to increase until a plateau, superimposed by pronounced oscillations at 445 and 550 N is reached, respectively. In case of the impact at 4.5 $^{\mathrm{m}}/_{\mathrm{s}}$, the force begins to rise again at a deflection of 2 mm until the global maximum is reached slightly below 3 mm. From that point on, force levels begin to decrease until the impactor reaches its reversal point at 4 mm and 400 N. During the impact at 6.0 $^{\mathrm{m}}/_{\mathrm{s}}$, the oscillations around the plateau are more pronounced. It continues up to a deflection of 4 mm, at which point the force begins to decrease, without a prior increase. Notably, this decrease in force continues up to 7 mm, at which point the reversal occurs with 200 N, far lower than at 4.5 $^{\mathrm{m}}/_{\mathrm{s}}$. After the reversal, the impactor is repelled with continuously decreasing force, again subjected to oscillations.

After an initial non-linear deceleration during which the contact is established, the impactor's tip velocity decreases with constant acceleration up to the point of first failure at 0.0015 s. Following that, changes in velocity gradually decelerate up to the repulsion of the impactor at 2.87 and 2.31 $^{\mathrm{m}}/_{\mathrm{s}}$, respectively.

4. Comparison of model predictions and experimental results

The constitutive model's behavior is verified by numerically analyzing the conducted experiments using two implementations with explicit time integration. Firstly, the uniaxial case is implemented using Python, allowing for a rapid and flexible analysis of test cases with uniaxial stress states. Secondly, the full 3D constitutive model is implemented as Abaqus/Explicit `VUMAT`, enabling the analysis of the material response under arbitrary loading conditions.

4.1. Model results for parameter identification experiments

PI experiments are set up in a way that only one stress component significantly deviates from zero. Therefore they can efficiently be analyzed using the Python implementation, in which the experimental boundary conditions (BCs) can be directly incorporated. Alternatively, the undisturbed region of the specimen can be represented by a single element test (SET) with appropriate BCs, when assuming ideal fiber alignment and small deformations.

For the displacement controlled deformation steps, permanent comparison of the current deformation, with the target value was necessary, since the occurring plastic deformation cannot be known in advance. The deformation state was obtained from a nodal `*SENSOR` for every time increment. Once the target value was reached, the step was prematurely ended by setting `lFlagsDefine(iConcludeStep) = 1`. Since the usage of `VUAMP` prevents the definition of relative changes in acting forces [65] and the absolute values at the end of each retardation period cannot be known a priori, unloading is modeled by prescribing a nodal velocity that leads to the same strain rate as the one during loading. Similar to the loading steps, nodal force from `*SENSOR` was monitored constantly and the step was stopped once the force value reached zero. Additionally, the material's density was increased by a factor of 1.5e3 to achieve a stable time increment of 1e-6 s during loading and unloading, which has been shown in preliminary tests to not affect the predicted stress-strain response. A factor of 1.5e6 has been used for relaxation and retardation periods, leading to a stable time increment of 1e-3 s. Using this increased density, simulations took 12 h on an AMD Ryzen 7 PRO 4750U using 1 core.[3] The resulting stress-strain curves are juxtaposed with the experimental results in Fig. 11.

Both under transverse tension as well as shear loading, the model shows good agreement with the experimental results both during the loading as well as the relaxation period. During the unloading and subsequent retardation the simulations exhibit some principal deviations that increase with the overall deformation. This stems from the fact that the model was solely developed and fitted to the relaxation behavior. Given the specialization of the Python implementation, it allows for an adaptation of the viscoelastic parameters solely for unloading and retardation, thus taking the fundamental change from tensile to compressive viscoelastic stress into account, without adding significant complexity to the overall model.[4] Here, a second set of parameters has been determined with a focus on correctly predicting the deformation at the end of the retardation period, since this influences subsequent steps the most. The parameters are given in Table 4, respective curves are shown in Fig. 11. Under both loading conditions the inelastic deformation remains so small throughout the first cycles that both models produce very similar results. With increasing inelastic deformation and the accumulation of deviations in the Abaqus model however, the adjusted model deviates more noticeably. It remains in far better agreement with the experimental results, throughout all cycles. In order to tackle the remaining deviations during unloading, the strain rate dependent part of the constitutive model would have to be adapted.

4.2. Model results for validation experiments

The predictive capabilities of the developed models are investigated by simulation of additional loading conditions that were not used for PI. In doing so, extrapolation in terms of total deformation and strain rate is

---

[3] For the investigated SETs, parallelization overhead was larger than simulation speed-up.

[4] To differentiate between loading and unloading in the general model, the definition of a viscoelastic potential and application of Kuhn–Tucker conditions could be a solution.

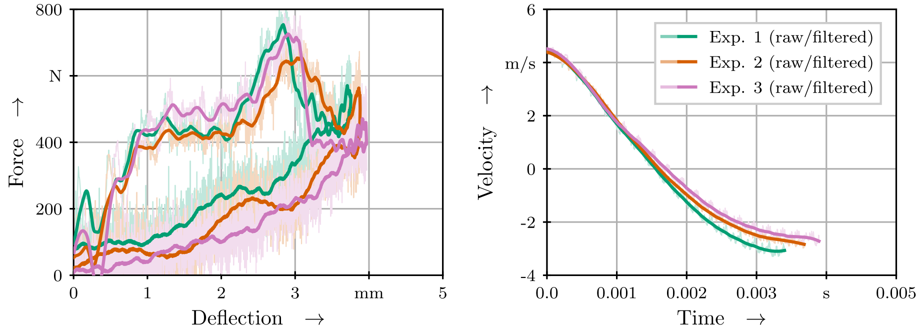

(a) Force-displacement at $v_{\mathrm{imp}} = 4.5\,\mathrm{m/s}$ (b) Velocity-time at $v_{\mathrm{imp}} = 4.5\,\mathrm{m/s}$

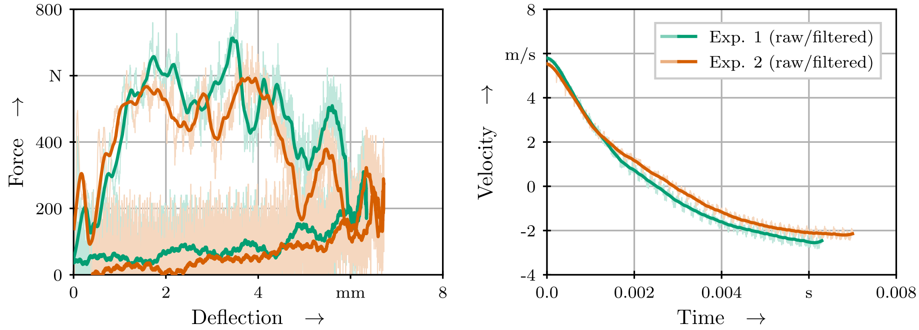

(c) Force-displacement at $v_{\mathrm{imp}} = 6.0\,\mathrm{m/s}$ (d) Velocity-time at $v_{\mathrm{imp}} = 6.0\,\mathrm{m/s}$

Fig. 10. Material response to impacts with different velocities.

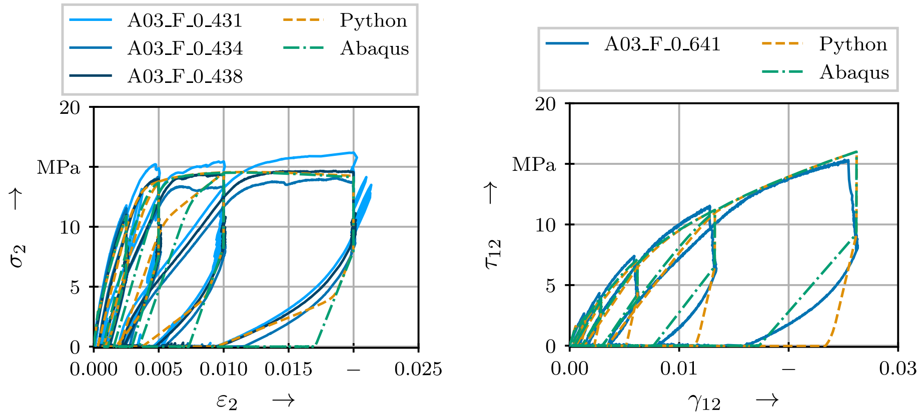

(a) Transverse Tension ($\dot{\varepsilon} = 1.2\mathrm{e}{-4}\,1/\mathrm{s}$) (b) In-plane shear ($\dot{\gamma} = 2.0\mathrm{e}{-4}\,1/\mathrm{s}$)

Fig. 11. Simulation results from tests with stepwise loading and unloading with relaxation and retardation periods.

investigated as well as interaction between the fundamental deformation modes by means of off-axis specimens.

In order to assess the predictive capabilities of the model, at first transverse tension and in-plane shear tests with continuous loading are investigated. The former are compared up to a strain $\varepsilon = 0.04$, twice the PI range, the latter for the valid shear strain range until 5 %, as per [62]. Given the 1D stress state, analyses are carried out using the Python implementation. For the comparison between experimental and simulated data, the effect of pre-tensioning has been removed from experimental data.

Experimental results and simulation predictions for testing velocities of 1 and 16 $^{\mathrm{mm}}/_{\mathrm{min}}$ are juxtaposed in Fig. 12. At both testing velocities, the developed model accurately captures the initial stiffness and onset of significant non-linearities. At 1 $^{\mathrm{mm}}/_{\mathrm{min}}$, the model predicts a soft stress maximum at $\varepsilon = .011$ and slow stress decrease with increasing deformation after that, as opposed to the plateau like behavior in the experimental curves. Nevertheless, the simulation results remain in very good agreement with experimental observations throughout the entire strain range. At 16 $^{\mathrm{mm}}/_{\mathrm{min}}$, the decrease in predicted stress is less pronounced, leading to an even better agreement between experiment and simulation.

Fig. 13 contains the similar comparisons under in-plane shear. At the quasi-static testing velocity, experiments and model are in complete agreement throughout the deformation range used for PI ($\gamma = 2.62$ %, c.f. Table 2). Under continuous loading, the agreement is even better than observed in the PI experiments, further emphasizing that the small previous discrepancies stem from the unloading behavior and the simplification of equating relaxation and retardation. If the model is used

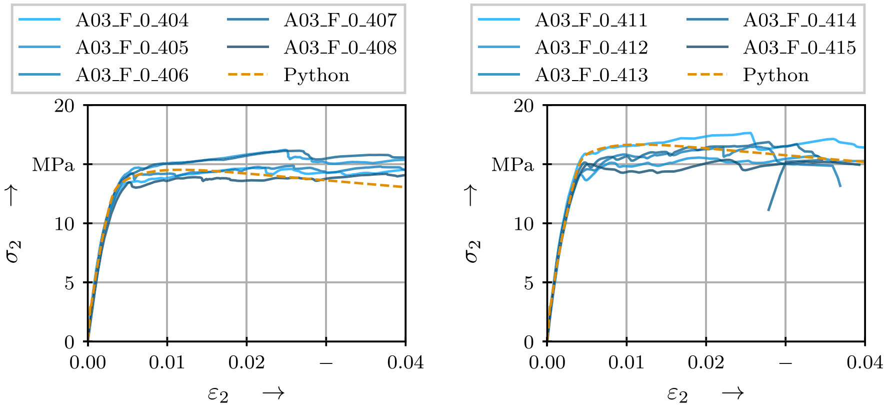

(a) Testing velocity of 1 mm/min ($\dot{\varepsilon} = 1.1\mathrm{e}{-4}\,1/\mathrm{s}$) (b) Testing velocity of 16 mm/min ($\dot{\varepsilon} = 2.2\mathrm{e}{-3}\,1/\mathrm{s}$)

Fig. 12. Validation experiments with $[90°]_4$ layup for transverse tension with belonging simulated curves.

to extrapolate the prediction of material behavior up to the final strain of the experiment, close to twice what was used for PI, minor deviations arise that slightly increase with the extrapolation distance but remain within a highly satisfactory range. The model behavior suggests that after exceeding the calibration limit, an acceleration of inelastic deformation and stiffness degradation takes place. However, the exact cause of this cannot be determined experimentally, since it would require prolonged holding close to the material's failure strain which is not feasible.

To further investigate the model's extrapolative capabilities, experiments performed at the increased testing velocities of $16^{\mathrm{mm}}/_{\mathrm{min}}$ and $100^{\mathrm{mm}}/_{\mathrm{min}}$ are used. This, again, leads to an excellent agreement between experiments and model predictions well past the range used for the underlying PI at $1^{\mathrm{mm}}/_{\mathrm{min}}$, without significant deviation up to a deformation of $\gamma = 3.5$ %. Continued model extrapolation up to $\gamma = 5$ % yields good agreement with the experiments, as was the case in the previous experiment. The continued good agreement between model predictions and experiments, both when extrapolating to larger strains as well as higher strain rates, verifies the predictive capabilities of the proposed model.

Interaction between the two investigated deformation modes of transverse and shear deformation is analyzed by using test specimen with a $[30°_2/-60°_2]_s$ layup. The model prediction for the resulting multi-axial stress state is obtained using the Abaqus implementation. The number of elements in the FEA model is kept as small as possible, in order to allow for the analysis of the extremely long loading-unloading experiments, where a physical time of 50 h has to be simulated using explicit time integration. Hence, the specimen is abstracted to a cube of side length 1 mm, which is partitioned into the four layers, each with a thickness of 0.25 mm. Each layer is represented by a single fully integrated element, as preliminary studies showed significant hourglassing when using reduced elements. The resulting mesh has four elements of type C3D8. No translation is allowed on the three base sides of the cube, preventing rigid body motion while allowing for lateral contraction. However, this approach cannot capture typical "double S" type deformation of unbalanced ply layups. Since more accurate geometric representations of the test set-up would make simulation time infeasibly long, this numerically highly efficient representation of the specimen is used for subsequent analyses. The suppression of the "double S" deformation may lead to a virtual stiffening of the simulation, however, because deformation at failure is small, the effect is considered negligible. Axial stress from simulation is calculated using

$$\sigma = \frac{1}{A_{\mathrm{sim}}} \sum_i F^i \quad , \tag{39}$$

with nodal forces F^i at nodes i of the face with translational BCs and FEA-model cross section A_{sim}.

Firstly, the quasi-static test with continuous loading is simulated with a longitudinal strain rate equivalent to the experimental one. Simulation results are shown in Fig. 14 alongside the experimental curves. Excellent agreement of this model extrapolation may be observed throughout a significant range of the deformation, validating the assumption that suppression of the "double S" deformation does not significantly influence the behavior here. Both the initial slope as well as the course of the curve up to a strain of 0.02 coincide with the experimental findings. From that deformation state onward, the extrapolative deviations observed for the in-plane shear behavior begin to affect these simulation results as well. This leads to an overestimation of the increase in reaction force. Still, the deviations up to the total failure of the specimen are within an acceptable range. The failure itself and potential modeling approaches have not been part of this investigation.

During the stepwise testing, the model predictions slightly underestimate experimentally observed forces during both loading phases. However, the equilibrium force after the relaxation period is in excellent agreement. This indicates that the previous underestimation stems from the viscoelastic overstress. It could therefore be a consequence of the simplified modeling of strain rate dependency, where lateral contraction or prevention thereof currently does not contribute to stress build-up. Unloading and retardation match extremely well. The absence of deviations as opposed to the PI-experiments can be attributed to the comparatively small deformation state. During the PI-experiments, deviation increased with overall deformation state. Altogether, the model was capable of predicting experimental behavior, for the combination of a layup and testing velocity not used during PI, with high accuracy.

To further investigate the influence of the individual modeling aspects, additional simulations of the validation case with stepwise loading and unloading only taking specific aspects of the derived model into account are carried out. In Fig. 15 evolution of strain and stress over time as well as stress-strain-curves are shown, each superimposed with the experimental results.

From the stress response during the relaxation periods it becomes clear that the purely elastic model predicts far too high stress levels, which remain constant throughout the relaxation period. Taking viscoelastic effects into account, leads to initially even higher stress levels which mostly decay over the course of the 5 h relaxation period. Replacing viscoelasticity with pure CDM brings stress levels down to a more realistic level, similar to the state observed after relaxation. Further consideration of plasticity reduces the stress response slightly. However, in both cases the stress level remains constant for the entire relaxation period. Only the combination of viscoelasticity and damage

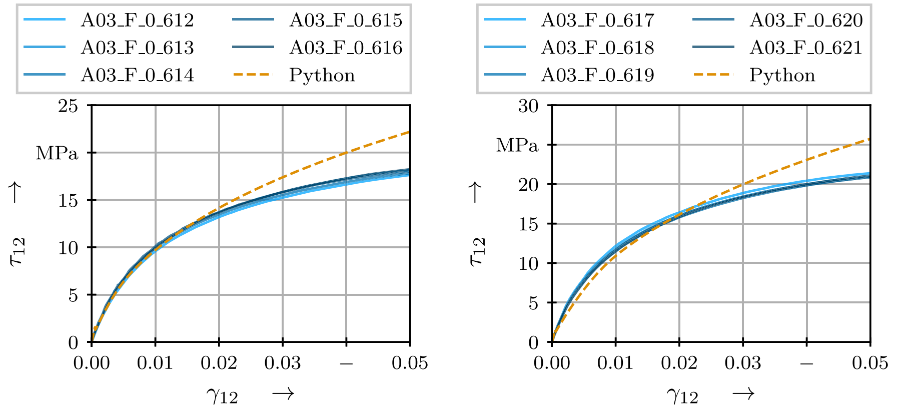

(a) Testing velocity of 1 mm/min ($\dot{\gamma} = 2.2\text{e}{-4}\,1/\text{s}$) (b) Testing velocity of 16 mm/min ($\dot{\gamma} = 3.6\text{e}{-3}\,1/\text{s}$)

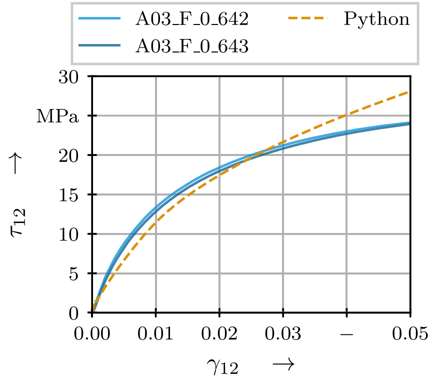

(c) Testing velocity of 100 mm/min ($\dot{\gamma} = 2.2\text{e}{-2}\,1/\text{s}$)

Fig. 13. Validation experiments with $[45^\circ_2/-45^\circ_2]_s$ layup for in-plane shear with respective simulation curves.

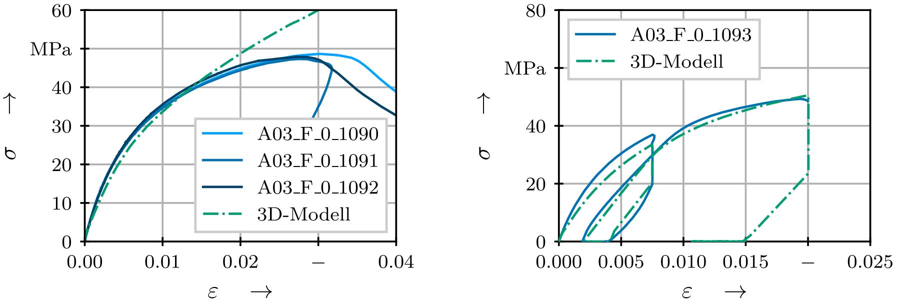

(a) Continuous loading at $\dot{\varepsilon} = 1.3\text{e}{-4}\,1/\text{s}$

(b) Stepwise loading and unloading with relaxation and retardation periods; loading at $\dot{\varepsilon} = 2.6\text{e}{-4}\,1/\text{s}$

Fig. 14. Validation experiments with $[30^\circ{}_2/{-60}^\circ{}_2]_s$ layup for deformation model interaction with respective simulation curves.

with or without plasticity allows for an accurate prediction of the initial stress peak at the end of loading and the subsequent decay towards an equilibrium.

Similarly, the purely elastic model does not capture the strain behavior during the retardation phase. It predicts an immediate drop to zero strain. The viscoelastic model gives a rapid drop in strain followed by a slow decay towards the initial geometry. For the deformation behavior, taking only CDM into account does not yield any effect. Identical to the purely elastic model, immediate restoration of the initial geometry after unloading is predicted. Adding viscoelasticity to CDM prevents the almost immediate change to the undeformed configuration. However, the predicted retardation exceeds the experimental observations, even the equilibrium behavior, for which the experimentally observed strain decay has to be extrapolated by 15 %. The pure plasticity model on the other hand gives an accurate estimate of this equilibrium behavior. However, just as the addition of CDM has resulted in a time-independent stress plateau, plasticity yields an immediate drop to a constant deformation state after unloading. Again, the predictions of the developed model are in excellent agreement with experimental observations.

Combining the insights from relaxation and retardation makes it clear that only a constitutive model taking viscoelasticity, CDM and plasticity into account can capture the intricate stress response and

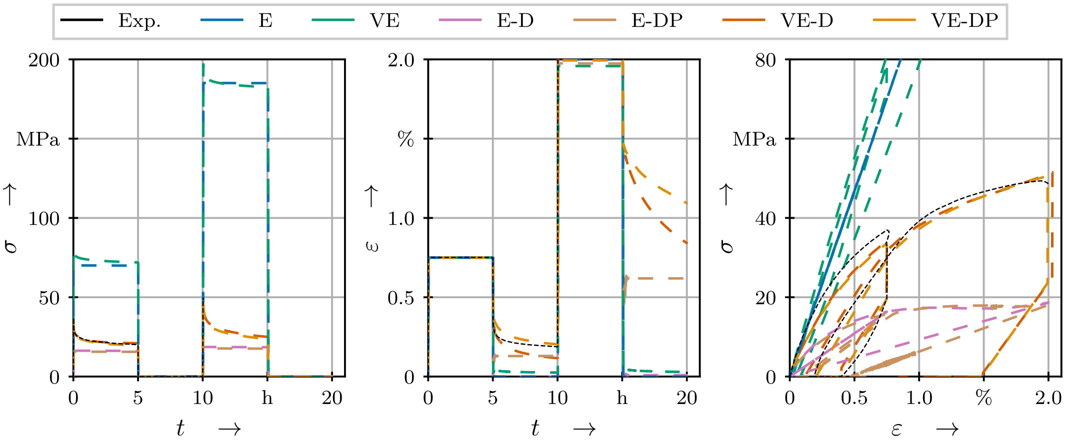

Fig. 15. Effect of modeling aspects on results for validation case (“E”: elastic, “VE”: viscoelastic, “D” with CDM, “P” with plasticity).

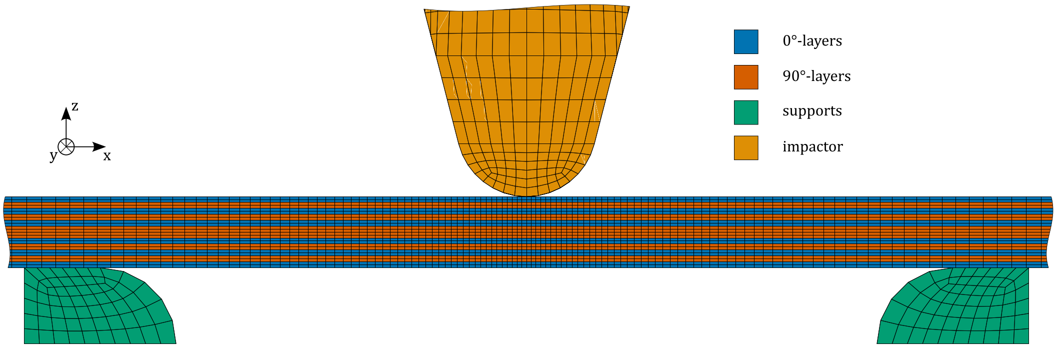

Fig. 16. Detailed view on impact region of initial FEA model for 3P-IB.

unloading behavior of the GF/PP. This is further emphasized by a comparison of the respective stress-strain curves with the experimental results. Only the VE-DP model accurately predicts the material behavior, including inelastic deformation, throughout the entire experiment well. All other models fail to capture essential aspects.

3 P-IB The 3 P-IB experiments are analyzed using Abaqus. The geometry of all parts is discretized using 3D continuum elements with reduced integration (`C3D8R`), resulting in the mesh of the impact region shown in Fig. 16. Across the entire specimen, cohesive zone models (CZMs) with a thickness of 1e-4 mm are added between all layers to account for potential delamination. This strategy has been shown to allow for an accurate assessment of the structural behavior of the used GF/PP in [66]. To determine suitable mesh size, a mesh convergence study was conducted. Details are given in Appendix F. The 0.25 mm thickness of each FRTs layer is discretized with 2 elements as a compromise between simulation accuracy and time. The region directly underneath the impactor is meshed with an edge length of 0.22 mm in the x-direction and 1 mm in y-direction. The latter does not require higher mesh density since both material as well as impact do not change in this direction. The mesh is coarsened in the x-direction towards the specimen edges up to an edge length of 1 mm. The resulting characteristics of the mesh are given in Table 5.

Table 5
Characteristics of FEA model for 3P-IB.

Part	Specimen	Impactor	Support
No. C3D8R	36,720	10,240	930
No. COH3D8	16,830	0	0

The developed constitutive model with determined parameters from Ref. [38] is used for each of the FRTs layers with a global orientation. Properties for the traction separation law are extrapolated from Ref. [67], where the same material with graded interface properties was studied. Used values are given in Table 6. Steel supports and titanium impactor are modeled as purely elastic to allow for propagation of stress waves and thus a more realistic representation of the impact system.

General contact with a coefficient of friction of 0.1 is defined among all exterior surfaces, with updates if elements are deleted. The contact is enforced based on penalty stiffness. The side of the supports facing away from the impactor is clamped and an initial velocity v_{imp} in the z-direction is applied to all nodes of the impactor. The simulation time is set to an arbitrarily large number, with termination criteria on displacement of the impactor tip, stopping the simulation once it has been repelled by more than 0.5 mm compared to its initial position. An explicit time integration scheme with default bulk viscosity parameters is chosen. Using an 6 cores on an i7-8700 CPU, this leads to wall clock times of 13.68, 26.41 and 31.24 h for the respective impact velocities of 4.5, 6.0 and 9.0 $^{\mathrm{m}}/_{\mathrm{s}}$.

Fig. 17 shows the deformation state and calculated out-of-plane shear stress τ_{23} in the specimen subjected to an impact with an initial velocity of 6 $^{\mathrm{m}}/_{\mathrm{s}}$ after 1.1e-3 s. A mode II driven delamination in the plane of symmetry on the left side of the specimen is clearly visible, leading to a local reduction in stress. Such asymmetric delaminations are commonly observed under three point bending in FRP, see e.g., [43,68,69]. Experimentally, these occur due to slight asymmetries in the specimen, both geometric as well as material properties, and imperfections in the load introduction. In simulation, it is also influenced by imperfections and round-offs. In both cases, this leads to marginally asymmetric stress

Table 6
Properties of CZM adapted from Ref. [67].

Property	E_3	$G_{12} = G_{23}$	R_I	$R_{II} = R_{III}$	$\mathcal{G}_{Ic}$	$\mathcal{G}_{IIc} = \mathcal{G}_{IIIc}$
Value	5600 MPa	2200 MPa	13. MPa	14. MPa	2.5 N/mm	1.81 N/mm

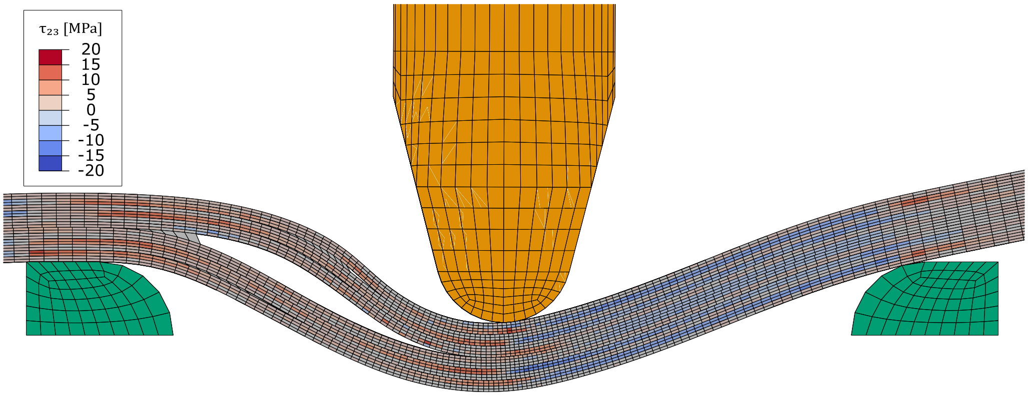

(a) Out-of-plane shear stress τ_{23} after 1.1e−3 s

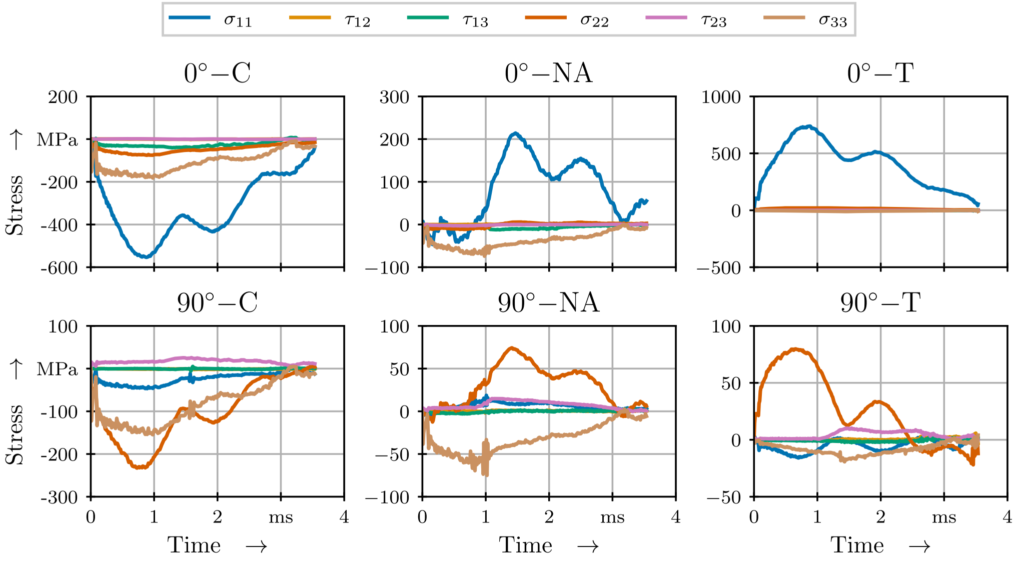

(b) Evolution of stress over time in different elements with 0° or 90° orientation dominated by **C**ompression or **T**ension, or close to **N**eutral **A**xis

Fig. 17. Multi-axiality of stress state in 3P-IB at 6 $^{\mathrm{m}}/_{\mathrm{s}}$.

distributions. Once delamination is initiated on the more critical side, some of the energy in the system is dissipated and overall stress levels drop. Therefore, the remaining internal energy is not critical with regard to initiating another delamination.

The calculated out-of-plane shear stress values in a range of ±20 MPa (τ_{23}) and ±40 MPa (τ_{13}) contribute significantly to the material's deformation resistance. To investigate this further, the evolution of individual stress components at three distinct locations along the middle of the specimen is analyzed, each time in one element with 0 ° orientation and one with 90 ° with respect to the primary axis of the specimen. First on the specimen's side close to the impactor, which is dominated by compressive stress (denoted by **C** in Fig. 17b), next close to the originally neutral axis (according to standard bending theory, denoted by **NA**) and finally on the far side, dominated by tensile stress (denoted by **T**). The 0 °-C element shows very high stress in the fiber direction, accompanied by significant contributions from both transverse normal stresses as well as through-thickness shear stress τ_{13}. In the 90 °-C element, transverse normal stress components reach an even higher level, with pronounced contributions from the τ_{23} shear component. With the initiation of delamination at 0.8 ms, the global bending stiffness of the specimen is reduced, initiating a decline in the normal stress component aligned with the specimen's primary direction (σ_{11} for 0 °-NA; σ_{22} for 90 °-NA). This is further superimposed by the dynamic behavior of the specimen, with free ends starting to pose additional deformation resistance at 1.4 ms, thus inducing an increase in the longitudinal stress components. At the neutral axis, the initial stress is dominated by compressive through-thickness stress σ_{33} as a result of the impact, superimposed by shear components τ_{13} and τ_{23} for 0 °-NA and 90 °-NA respectively. Here, the initiation of delamination leads to a buildup of additional longitudinal stress, which is subsequently also affected by the oscillations of the specimen's free ends. On the far side of the specimen, tensile stress in the fiber direction dominates the behavior of the

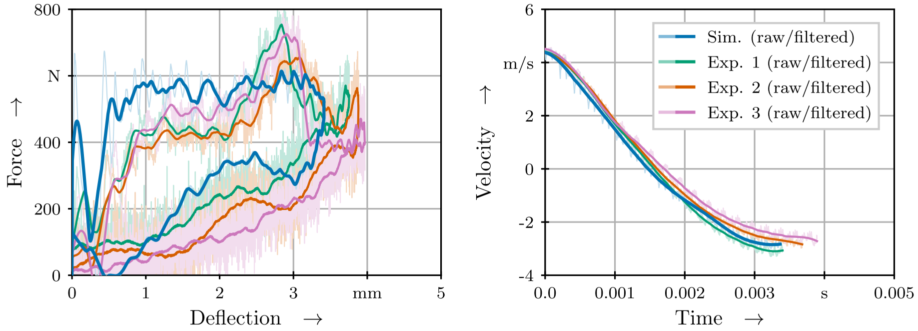

(a) Force-displacement at $v_{\mathrm{imp}} = 4.5\,\mathrm{m/s}$ (b) Velocity-time at $v_{\mathrm{imp}} = 4.5\,\mathrm{m/s}$

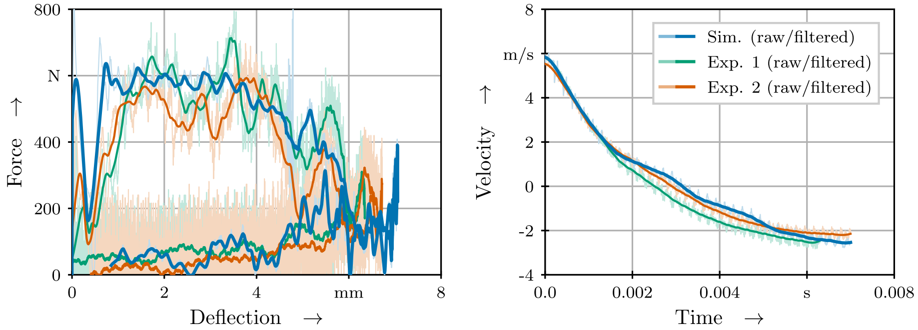

(c) Force-displacement at $v_{\mathrm{imp}} = 6.0\,\mathrm{m/s}$ (d) Velocity-time at $v_{\mathrm{imp}} = 6.0\,\mathrm{m/s}$

Fig. 18. Comparison of simulation and experimental response to 3P-IB at different velocities.

0 °-T element. Here, the effect of decrease in maximum stress due to the delamination may be observed as well. Similarly, σ_{22} in the 90 °-T element first rises and then declines. Additionally, transverse shear stress τ_{23} begins to build up at 1 ms. From the analysis of the stress evolution in these elements it becomes clear that the material behavior throughout the 3 P-IB test is strongly influenced by the 3D stress states and their interactions.

To enable quantitative comparison of experiment and simulation, force is extracted from contact force between the impactor and the specimen in the simulation, impactor tip displacement and velocity are taken as averages over the nodes in the cylindrical part of the impactor tip. Just as with the experimental results, curves obtained from simulation were filtered to reduce the significant noise level. Resulting curves are shown together with experimental results in Fig. 18.

From this it becomes clear that the initial spike in the force is significantly more pronounced in the simulation than in the experiment at both impact velocities. This can be attributed to the idealized geometries of impactor and specimen, which lead to the simultaneous establishment of a line of contact across the entire width of the specimen, as opposed to a slightly staggered procedure due to geometric imperfections. Additionally, it is worth emphasizing that the resulting force history is taken in the numerical simulations directly at the point of contact, whereas in the experiments an indirect measurement based on d'Alambert's analytical wave analysis was used. This implies possible sources of deviation due to dispersion and damping in the 3 P-IB set-up. At 4.5 $^{\mathrm{m}}/_{\mathrm{s}}$, the level of the first force plateau at 559 N is overestimated by 114 N, compared to the experimental average, and remains at that level up to the reversal point, not capturing the additional force increase beforehand. This mostly balances out, leading to a slight underestimation of the deflection at reversal with 3.41 to 3.87 mm and a good agreement in force of 520 to 490 N for simulation and experiment, respectively. The unloading path is similar, with a re-increase of force from 3 to 2.5 mm. Impactor tip velocity is in excellent agreement throughout the entire experiment and most notably at separation, indicating that despite the observed deviations in the force response, dissipated energy is predicted correctly.

At an impact velocity of 6.0 $^{\mathrm{m}}/_{\mathrm{s}}$, good agreement between simulation and experiment can be observed after the initial spike, with an average force level throughout the force plateau from 1 to 4 mm deflection of 583 (simulation) to 536 N (experiment). The decline of the force is captured well, up to a force at reversal of 266 to 220 N, with an overestimation of the deflection of 7.05 to 6.52 mm for simulation and experiment, respectively. Subsequent unloading paths are in good agreement. As with the results at 4.5 $^{\mathrm{m}}/_{\mathrm{s}}$, excellent agreement between impactor velocity from simulation and experiment can be observed.

5. Conclusion and outlook

To accurately predict the behavior of FRTs under arbitrarily complex loading conditions, a recently published material model has been extended to a 3D formulation. This enables the application of the constitutive model to further areas of active research. A key motivation is to improve the understanding of how manufacturing and mechanical joining methods influence load-bearing behavior by inducing complex 3D fiber orientations and associated stress states.

The extended model has been applied to a UD GF/PP. The identified parameters assuming transversely isotropic behavior in each UD ply are summarized in Table 4. Using these parameters, PI experiments have been analyzed using the developed 3D-model. It has been found to accurately represent the intricate material behavior during loading and relaxation periods. During the unloading phase, the simplifying assumption of identical viscoelastic behavior as under loading led to noticeable model deviations. Nevertheless, error accumulation for all loading sections remained insignificant throughout the analysis of up to five cycles in the used stepwise testing procedure. It has been shown, that simple adjustments such as using separate parameter combinations for the viscoelastic behavior during loading and unloading to take the change from tensile to compressive behavior into account can further improve the prediction accuracy.

Predictive performance was determined by a variety of validation tests not used for PI. For tests with continuously increasing deformation, extrapolation up to twice the strain used during PI showed overall excellent agreement with experimental results. This accuracy could be extended to significantly increased testing velocity both under transverse tension as well as in-plane shear. Additionally, model predictions for the interaction between these two loading conditions were in very close agreement with experimental observations from off-axis specimens, both under continuous as well as stepwise loading.

The influence of the individual modeling aspects was elucidated using the example of the off-axis tests with loading, relaxation, unloading and retardation. This comparison made it clear that only a constitutive model taking viscoelasticity, CDM and plasticity into account can capture the intricate behavior of GF/PP undergoing non-monotonous loading.

Finally, the generalization capabilities of the developed model were demonstrated by its application to several low-velocity impact scenarios, with local strain rates reaching up to 100 $^1/_s$. Under these conditions, far exceeding the calibration experiments, the specimens' force-deflection responses were predicted with some compromises at an impact velocity of 4.5 $^m/_s$ and with very good agreement at 6.0 $^m/_s$. The impactor velocity at separation, indicating energy dissipated throughout the experiment, was captured with excellent agreement.

The proposed model constitutes a sound basis for the analysis of UD FRTs under complex geometric and loading conditions. It may well be applied to other transversely isotropic materials with similar behavioral characteristics, such as yarns in a mesoscopic modeling of woven fabrics. For this, the modularity of the proposed model may be leveraged to make necessary replacements of modeling aspects "in-place". Further development should focus on incorporating failure modes that lead to immediate structural failure without prior damage evolution. This would enable the analysis of impact events with even higher energy and crash experiments as well as joining tasks that locally cut the material, such as self piercing riveting. In this context, approaches that explicitly consider the complex interaction of superimposed stress states, such as our recent proposition [70], offer significant potential. In connection with this, a differentiation between loading and unloading behavior for the viscoelastic part represents a promising opportunity for model improvement. Finally, the actual application of the developed model to a joining zone with its complex local fiber architecture after mechanical joining is expected to enable deep insights into its load-bearing behavior, failure mechanisms and resulting optimization potential.

CRediT authorship contribution statement

Johannes Gerritzen: Writing – review & editing, Writing – original draft, Visualization, Validation, Software, Methodology, Investigation, Funding acquisition, Formal analysis, Data curation, Conceptualization. **Benjamin Gröger:** Writing – original draft, Investigation, Funding acquisition. **Matthias Zscheyge:** Writing – review & editing, Conceptualization. **Andreas Hornig:** Writing – review & editing, Validation, Supervision, Resources, Project administration, Funding acquisition. **Maik Gude:** Writing – review & editing, Supervision, Project administration, Funding acquisition.

Declaration of generative AI and AI-assisted technologies in the writing process

During the preparation of this work the authors used ChatGPT with model "4.5" in order to improve readability and language of the manuscript. After using this tool, the authors reviewed and edited the content as needed and take full responsibility for the content of the publication.

Funding

This research was funded by the Deutsche Forschungsgemeinschaft (DFG, German Research Foundation) – TRR 285/2 – 418701707 – subproject A03.

Declaration of competing interest

The authors declare that they have no known competing financial interests or personal relationships that could have appeared to influence the work reported in this paper.

Appendix A. Robustifying the implementation of stiffness loss under fiber parallel compression

Regarding the implementation of the stiffness loss factor it must be noted, that the standard approach for explicit time integration

$$\Gamma^{t+\mathrm{d}t} = 1 + \gamma \left\langle \sigma_1^t \right\rangle^{(-)} \tag{A.1}$$

leads to numerical instabilities, which intensify with reduction of the time increment dt as shown in Fig. A.19 for the example of applying a uniaxial compressive strain of $\bar{\varepsilon}_1 = -0.05$ in a virtual time of 1 s.

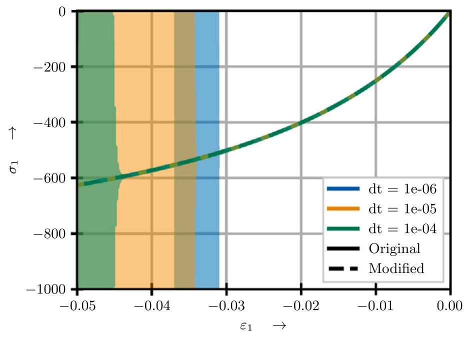

Fig. A.19. Instabilities in the stress-strain behavior under uniaxial compression.

For the uniaxial case, this can be prevented by inserting the stress $\sigma_1 = E_1\,\Gamma\,\varepsilon_1$ into (3). The resulting equation can be rearranged, yielding

$$\Gamma = \frac{1}{1 - \gamma\, E_1\, \varepsilon_1} = \frac{1}{1 - \gamma\, \sigma_1^{lin}} \quad , \tag{A.2}$$

with the linear stress σ_1^{lin}, which would occur without the elastic stiffness loss. For the general case, the second definition of Γ is used, with the generalized linear stress $\sigma_1^{lin} = \left[\underline{\underline{\tilde{C}}}\Big|_{\Gamma=1} \; \varepsilon^{\mathrm{e}} \right]_1$. This leads to a small error, since the effects of fiber parallel compression on the Poisson ratios (c.f. Eq. (4)) were neglected in the derivation. Taking the effects into account, however, would prohibit an analytical solution, thus also introducing errors and adding significant complexity to the model from approximations of the solution. The presented solution has been found to be stable under all investigated loading conditions.

Appendix B. Derivation of relationship between plastic multiplier $\dot{\lambda}$ and effective equivalent plastic strain rate $\dot{\tilde{\varepsilon}}_e^p$

Given the effective equivalent stress from Eq. (16)

$$\tilde{\sigma}_e = \sqrt{\left(\underline{\underline{D}}\,\underline{\sigma}\right)^T \underline{\underline{A}}\,\underline{\underline{D}}\,\underline{\sigma}}$$

and yield criterion Eq. (19)

$$f = \tilde{\sigma}_e - Y = 0$$

for the derivative

$$\frac{\partial f}{\partial \underline{\sigma}} = \frac{\underline{\underline{D}}\,\underline{\underline{A}}\,\underline{\underline{D}}\,\underline{\sigma}}{\tilde{\sigma}_e}$$

follows. Substituting this and the definition for plastic strain rate from the associative flow Eq. (20)

$$\underline{\dot{\varepsilon}}^p = \dot{\lambda}\,\frac{\partial f}{\partial \underline{\sigma}}$$

into part I of the rate of plastic work from Eq. (22)

$$\dot{W}^p = \underbrace{\underline{\sigma}^T\,\underline{\dot{\varepsilon}}^p}_{I} = \underbrace{\tilde{\sigma}_e \dot{\tilde{\varepsilon}}^p_e}_{II}$$

yields

$$\underline{\sigma}^T\,\dot{\lambda}\,\frac{\underline{\underline{D}}\,\underline{\underline{A}}\,\underline{\underline{D}}\,\underline{\sigma}}{\tilde{\sigma}_e} \iff \dot{\lambda}\,\underline{\sigma}^T\,\frac{\underline{\underline{D}}\,\underline{\underline{A}}\,\underline{\underline{D}}\,\underline{\sigma}}{\tilde{\sigma}_e} \iff \dot{\lambda}\,\frac{\tilde{\sigma}_e^2}{\tilde{\sigma}_e} \iff \dot{\lambda}\tilde{\sigma}_e \quad .$$

Equating I and II gives

$$\dot{\lambda}\tilde{\sigma}_e = \tilde{\sigma}_e \dot{\tilde{\varepsilon}}^p_e \quad ,$$

and hence

$$\dot{\lambda} = \dot{\tilde{\varepsilon}}^p_e \quad . \tag{B.1}$$

Appendix C. Derivation of effective equivalent plastic strain rate under transversely isotropic assumptions without plasticity in primary direction

Based on the definition of the effective stress for transverse isotropy in Eq. (16)

$$\tilde{\sigma}_e = \sqrt{\left(\tilde{\sigma}_2 - \tilde{\sigma}_3\right)^2 + \left(\frac{R_2\,\tilde{\tau}_{23}}{R_{23}}\right)^2 + \left(\frac{R_2}{R_{12}}\right)^2 \left(\tilde{\tau}_{13}^2 + \tilde{\tau}_{12}^2\right)}$$

and flow rule (19)

$$f = \tilde{\sigma}_e - Y = 0 \quad ,$$

the directions of plastic strain can be written as

$$\frac{\partial f}{\partial \sigma} = \frac{1}{\tilde{\sigma}_e}\left[\ 0,\quad \frac{\tilde{\sigma}_2 - \tilde{\sigma}_3}{1-d_2},\quad \frac{\tilde{\sigma}_3 - \tilde{\sigma}_2}{1-d_2},\quad \left(\frac{R_2}{R_{23}}\right)^2 \frac{\tilde{\tau}_{23}}{1-d_2},\quad \left(\frac{R_2}{R_{12}}\right)^2 \frac{\tilde{\tau}_{13}}{1-d_{12}},\quad \left(\frac{R_2}{R_{12}}\right)^2 \frac{\tilde{\tau}_{12}}{1-d_{12}}\ \right] \quad . \tag{C.1}$$

Substituting this into the definition for effective plastic strain rate from the associative flow Eq. (21)

$$\underline{\dot{\tilde{\varepsilon}}}^p = \dot{\lambda}\,\frac{\partial f}{\partial \underline{\tilde{\sigma}}} = \dot{\lambda}\,\underline{\underline{D}}^{-1}\,\frac{\partial f}{\partial \underline{\sigma}} = \underline{\underline{D}}^{-1}\,\underline{\dot{\varepsilon}}^p .$$

and solving for the stress components yields

$$\tilde{\sigma}_2 - \tilde{\sigma}_3 = (1 - d_2)\,\frac{\tilde{\sigma}_e}{\dot{\lambda}}\left(\frac{\dot{\varepsilon}^p_2 - \dot{\varepsilon}^p_3}{2}\right) = \frac{\tilde{\sigma}_e}{\dot{\lambda}}\left(\frac{\dot{\tilde{\varepsilon}}^p_2 - \dot{\tilde{\varepsilon}}^p_3}{2}\right) \tag{C.2}$$

$$\tilde{\tau}_{23} = (1 - d_2)\,\frac{\tilde{\sigma}_e}{\dot{\lambda}}\,\frac{R_{23}^2}{R_2^2}\,\dot{\gamma}^p_{23} = \frac{\tilde{\sigma}_e}{\dot{\lambda}}\,\frac{R_{23}^2}{R_2^2}\,\dot{\tilde{\gamma}}^p_{23} \tag{C.3}$$

$$\tilde{\tau}_{13} = (1 - d_{12})\,\frac{\tilde{\sigma}_e}{\dot{\lambda}}\,\frac{R_{12}^2}{R_2^2}\,\dot{\gamma}^p_{13} = \frac{\tilde{\sigma}_e}{\dot{\lambda}}\,\frac{R_{12}^2}{R_2^2}\,\dot{\tilde{\gamma}}^p_{13} \tag{C.4}$$

$$\tilde{\tau}_{12} = (1 - d_{12})\,\frac{\tilde{\sigma}_e}{\dot{\lambda}}\,\frac{R_{12}^2}{R_2^2}\,\dot{\gamma}^p_{12} = \frac{\tilde{\sigma}_e}{\dot{\lambda}}\,\frac{R_{12}^2}{R_2^2}\,\dot{\tilde{\gamma}}^p_{12} \quad . \tag{C.5}$$

Substituting these equations into the effective stress, leads to

$$\tilde{\sigma}_e = \left\{\left[\frac{\tilde{\sigma}_e}{\dot{\lambda}}\left(\frac{\dot{\tilde{\varepsilon}}^p_2 - \dot{\tilde{\varepsilon}}^p_3}{2}\right)\right]^2 + \left(\frac{R_2\,\tilde{\sigma}_e\,R_{23}^2\,\dot{\tilde{\gamma}}^p_{23}}{\dot{\lambda}\,R_2^2\,R_{23}}\right)^2 \right.$$
$$\left. + \left(\frac{R_2}{R_{12}}\right)^2 \left[\left(\frac{\tilde{\sigma}_e}{\dot{\lambda}}\,\frac{R_{12}^2\,\dot{\tilde{\gamma}}^p_{13}}{R_2^2}\right)^2 + \left(\frac{\tilde{\sigma}_e}{\dot{\lambda}}\,\frac{R_{12}^2\,\dot{\tilde{\gamma}}^p_{12}}{R_2^2}\right)^2\right]\right\}^{\frac{1}{2}} . \tag{C.6}$$

Since $\frac{\tilde{\sigma}_e}{\dot{\lambda}}$ is quadratic in every term, it can be removed from the root and transferred to the other side of the equation. From eliminating redundancies in the fractions and taking Eq. (B.1)

$$\dot{\lambda} = \dot{\tilde{\varepsilon}}^p_e \quad .$$

into account,

$$\dot{\tilde{\varepsilon}}^p_e = \sqrt{\left(\frac{\dot{\tilde{\varepsilon}}^p_2 - \dot{\tilde{\varepsilon}}^p_3}{2}\right)^2 + \left(\frac{R_{23}}{R_2}\right)^2 \left(\dot{\tilde{\gamma}}^p_{23}\right)^2 + \left(\frac{R_{12}}{R_2}\right)^2 \left(\left(\dot{\tilde{\gamma}}^p_{13}\right)^2 + \left(\dot{\tilde{\gamma}}^p_{12}\right)^2\right)} \tag{C.7}$$

follows for the effective equivalent plastic strain rate.

Appendix D. Experimental results from tensile tests parallel to fiber direction

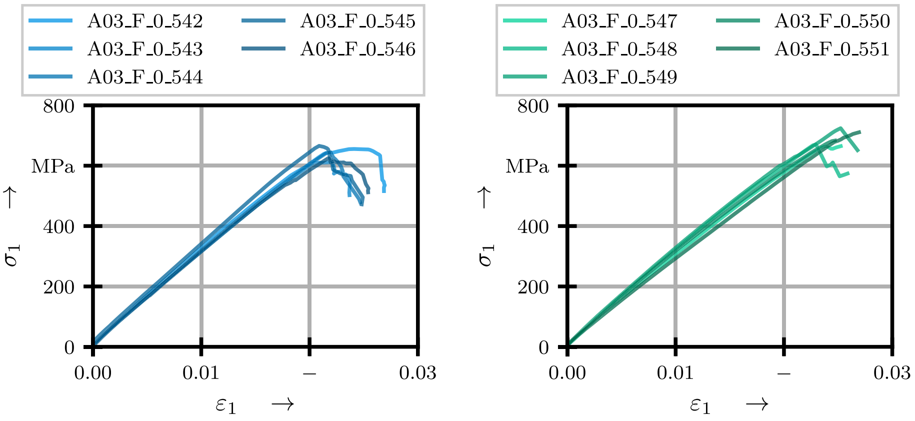

(a) Parallel Tension – $[0°]_4$; $v = 1\,\mathrm{mm/min}$

(b) Parallel Tension – $[0°]_4$; $v = 16\,\mathrm{mm/min}$

Fig. D.20. Experimental results from tensile tests parallel to fiber direction.

Appendix E. Results of 3P-IB tests performed at 9 $^{\mathrm{m}}/_{\mathrm{s}}$

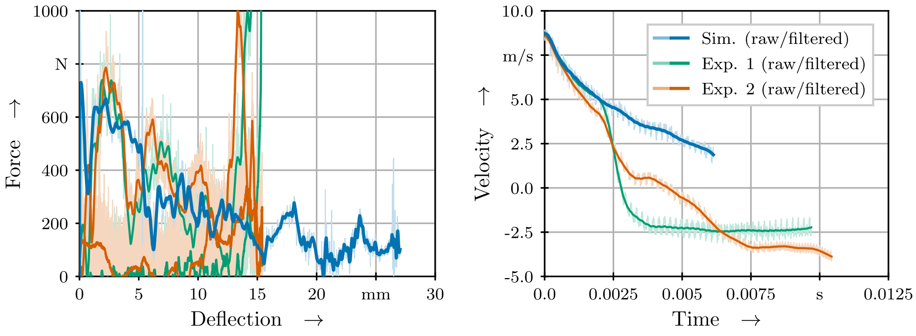

(a) Force-displacement

(b) Velocity-time

Fig. E.21. Experimental results from 3 P-IB tests at $v_{\mathrm{imp}} = 9.0\ ^{\mathrm{m}}/_{\mathrm{s}}$.

Appendix F. Mesh convergence study for 3P-IB simulation

To determine the influence of mesh size on simulation results, three discretizations were analyzed for the 3 P-IB at 4.5 $^{\mathrm{m}}/_{\mathrm{s}}$. Firstly, a *coarse* mesh with an element edge length in the primary direction of the specimen of 0.61 mm directly underneath the impactor, gradually coarsening up to 3.81 mm at the end of the specimen and 3 mm in the width direction, combined with one element across the thickness of each ply. This leads to a total of 3036 elements in the mesh. Secondly, a mesh with *medium* refinements, leading to an edge length of 0.40 mm in the middle of the specimen with coarsening up to 2 mm and 1.8 mm across the specimen width. This mesh also has one element across each ply, leading to a total of 9775 elements. And finally, a *fine* mesh with 0.22 mm edge length in the middle and 1 mm at the end of the specimen as well as across its width. This is combined with two elements across each ply, resulting in a total of 53,550 elements. Resulting force-time plots are shown in Fig. F.22.

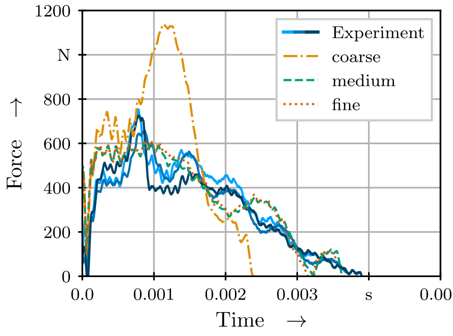

Fig. F.22. Influence of mesh size on predicted behavior.

From the comparison it becomes clear that the coarse mesh leads to significant deviations. With increasing mesh density, its influence decreases. To ensure that stress distribution across the individual plies can be captured by the model, the *fine* mesh is chosen for this work (Fig.E.21).

Data availability

Data is available upon request from https://trr285.uni-paderborn.de/en/publications.

References

[1] G. Jogur, A.N. Khan, A. Das, P. Mahajan, R. Alagirusamy, Impact properties of thermoplastic composites, Text. Prog. 50 (3) (2018) 109–183, https://doi.org/10.1080/00405167.2018.1563369

[2] J. Kim, M. Jeong, H. Böhm, J. Richter, N. Modler, Experimental investigation into static and dynamic axial crush of composite tubes of glass-fiber mat/PA6 laminates, Compos. Part B: Eng. 181 (2020) 107590, https://doi.org/10.1016/j.compositesb.2019.107590

[3] H. Böhm, J. Richter, J. Kim, G. Joo, H.-K. Jang, M. Jeong, A. Hornig, M. Gude, Glass-fiber mat/pa6 composite tubes subjected to dynamic axial crush loading—experimental evaluation and high fidelity modeling of failure phenomena, Composite Struct. 319 (2023) 117115

[4] A.R. Offringa, Thermoplastic composites—rapid processing applications, Compos. Part A Appl. Sci. Manuf. 27 (4) (1996) 329–336, https://doi.org/10.1016/1359-835x(95)00048-7

[5] A. Galińska, C. Galinski, Mechanical joining of fibre reinforced polymer composites to metals—a review. Part II: riveting, clinching, non-adhesive form-locked joints, pin and loop joining, Polymers 12 (2020) 1681, https://doi.org/10.3390/polym12081681

[6] B. Gröger, J. Troschitz, J. Vorderbrüggen, C. Vogel, R. Kupfer, G. Meschut, M. Gude, Clinching of thermoplastic composites and metals—a comparison of three novel joining technologies, Materials 14 (9) (2021) 2286, https://doi.org/10.3390/ma14092286.

[7] R. Bernatas, S. Dagreou, A. Despax-Ferreres, A. Barasinski, Recycling of fiber reinforced composites with a focus on thermoplastic composites, Clean. Eng. Technol. 5 (2021) 100272, https://doi.org/10.1016/j.clet.2021.100272

[8] M. Gude, C. Vogel, B. Gröger, Simulation-aided development of a robust thermoclinching joining process for hybrid structures with textile reinforced thermoplastic composites and metallic components, Materwiss. Werkst. 50 (8) (2019) 1027–1038, https://doi.org/10.1002/mawe.201900036

[9] B. Schramm, S. Martin, C. Steinfelder, C.R. Bielak, A. Brosius, G. Meschut, T. Tröster, T. Wallmersperger, J. Mergheim, A review on the modeling of the clinching process chain - Part I: Design Phase, J. Adv. Join. Process. 6 (2022) 100133, https://doi.org/10.1016/j.jajp.2022.100133

[10] R. Kupfer, L. Schilling, S. Spitzer, M. Zichner, M. Gude, Neutral lightweight engineering: a holistic approach towards sustainability driven engineering, Discover Sustainability 3 (1) (May 2022) https://doi.org/10.1007/s43621-022-00084-9

[11] M. Heibeck, M. Rudolph, N. Modler, M. Reuter, A. Filippatos, Characterizing material liberation of multi-material lightweight structures from shredding experiments and finite element simulations, Min. Eng. 172 (2021) 107142, https://doi.org/10.1016/j.mineng.2021.107142

[12] L.M. Kachanov, Rupture time under creep conditions (in Russian), Izv. Akad. Nauk SSSR (8) (1958) 26–31.

[13] Y.N. Rabotnov, Creep rupture, In M. Hetényi, W.G. Vincenti (Eds.), Applied Mechanics, Springer Berlin Heidelberg, Berlin, Heidelberg, 1969, pp. 342–349, https://doi.org/10.1007/978-3-642-85640-2_26.

[14] P. Ladevèze, E. LeDantec, Damage modelling of the elementary ply for laminated composites, Compos. Sci. Technol. 43 (3) (1992) 257–267, https://doi.org/10.1016/0266-3538(92)90097-M

[15] R. Talreja, A continuum mechanics characterization of damage in composite materials, Proc. R. Soc. Lond. Ser. A Math. Phys. Sci. 399 (1817) (1985) 195–216, http://www.jstor.org/stable/2397688.

[16] M. Salavatian, L.V. Smith, An investigation of matrix damage in composite laminates using continuum damage mechanics, Comp. Struct. 131 (2015) 565–573, https://doi.org/10.1016/j.compstruct.2015.06.012

[17] J. Ge, C. He, J. Liang, Y. Chen, D. Fang, A coupled elastic-plastic damage model for the mechanical behavior of three-dimensional (3D) braided composites, Compos. Sci. Technol. 157 (2018) 86–98, https://doi.org/10.1016/j.compscitech.2018.01.027

[18] Z. Hashin, Failure criteria for unidirectional fiber composites, J. Appl. Mech. 47 (2) (1980) 329–334, https://doi.org/10.1115/1.3153664

[19] H. Singh, K.K. Namala, P. Mahajan, A damage evolution study of E-glass/epoxy composite under low velocity impact, Compos. Part B Eng. 76 (2015) 235–248, https://doi.org/10.1016/j.compositesb.2015.02.016

[20] K.J. Park, H.-J. Kang, I.-H. Choi, S. Shin, S.J. Kim, Progressive failure analysis of carbon-fiber reinforced polymer (CFRP) laminates using combined material nonlinear elasticity and continuum damage mechanics based on treatment of coupon test, J. Compos. Mater. 50 (11) (2016) 1431–1455, https://doi.org/10.1177/0021998315592006

[21] C. Furtado, G. Catalanotti, A. Arteiro, P.J. Gray, B.L. Wardle, P.P. Camanho, Simulation of failure in laminated polymer composites: building-block validation, Comp. Struct. 226 (2019) 111168, https://doi.org/10.1016/j.compstruct.2019.111168

[22] H. Fallahi, F. Taheri-Behrooz, Phenomenological constitutive modeling of the non-linear loading-unloading response of UD fiber-reinforced polymers, Comp. Struct. 292 (2022) 115671, https://doi.org/10.1016/j.compstruct.2022.115671

[23] I.R. Cózar, F. Otero, P. Maimí, E.V. González, S. Miot, A. Turon, P.P. Camanho, A three-dimensional plastic-damage model for polymer composite materials, Compos. Part A Appl. Sci. Manuf. 163 (2022) 107198, https://doi.org/10.1016/j.compositesa.2022.107198

[24] I.R. Cózar, F. Otero, P. Maimí, E.V. González, A. Turon, P.P. Camanho, An enhanced constitutive model to predict plastic deformation and multiple failure mechanisms in fibre-reinforced polymer composite materials, Comp. Struct. 330 (2024) 117696, https://doi.org/10.1016/j.compstruct.2023.117696

[25] P.T. Goncalves, A. Arteiro, N. Rocha, F. Otero, Modeling 3D transverse elasto-plastic damage of unidirectional fiber-reinforced polymer composites using a smeared crack approach, Int. J. Solids Struct. 286-287 (2024) 112568, https://doi.org/10.1016/j.ijsolstr.2023.112568

[26] P.T. Goncalves, A. Arteiro, N. Rocha, F. Otero, Coupled longitudinal and transverse damage modeling of fiber-reinforced polymers using a smeared crack approach, Int. J. Solids Struct. 311 (2025) 113252, https://doi.org/10.1016/j.ijsolstr.2025.113252

[27] C. Hoffarth, S.D. Rajan, R.K. Goldberg, D. Revilock, K.S. Carney, P. DuBois, G. Blankenhorn, Implementation and validation of a three-dimensional plasticity-based deformation model for orthotropic composites, Compos. Part A: Appl. Sci. Manuf. 91 (2016) 336–350, https://doi.org/10.1016/j.compositesa.2016.10.024

[28] A. Matzenmiller, J. Lubliner, R.L. Taylor, A constitutive model for anisotropic damage in fiber-composites, Mech. Mater. 20 (2) (1995) 125–152, https://doi.org/10.1016/0167-6636(94)00053-0

[29] C. Hoffarth, B. Khaled, L. Shyamsunder, S. Rajan, R. Goldberg, K. Carney, P. DuBois, G. Blankenhorn, Verification and validation of a three-dimensional orthotropic plasticity constitutive model using a unidirectional composite, Fibers 5 (1) (2017) 12, https://doi.org/10.3390/fib5010012

[30] S. Chen, L. Li, An anisotropic damage-plasticity constitutive model of continuous fiber-reinforced polymers, Polymers 16 (3) (2024) 334, https://doi.org/10.3390/polym16030334

[31] S. Treutenaere, F. Lauro, B. Bennani, T. Matsumoto, E. Mottola, Finite strain formulation of viscoelastic damage model for simulation of fabric reinforced polymers under dynamic loading, E.P.J. Web Conf. 94 (2015) 04011, https://doi.org/10.1051/epjconf/20159404011

[32] J. Fritsch, S. Hiermaier, G. Strobl, Characterizing and modeling the non-linear viscoelastic tensile deformation of a glass fiber reinforced polypropylene, Compos. Sci. Technol. 69 (14) (2009) 2460–2466, https://doi.org/10.1016/j.compscitech.2009.06.021

[33] J. Gerritzen, A. Hornig, B. Gröger, M. Gude, A data driven modelling approach for the strain rate dependent 3D shear deformation and failure of thermoplastic fibre reinforced composites: experimental characterisation and deriving modelling parameters, J. Compos. Sci. 6 (10) (2022) 318, https://doi.org/10.3390/jcs6100318

[34] J.-F. Chen, E.V. Morozov, A consistency elasto-viscoplastic damage model for progressive failure analysis of composite laminates subjected to various strain rate loadings, Comp. Struct. 148 (2016) 224–235, https://doi.org/10.1016/j.compstruct.2016.03.049

[35] M. Kerschbaum, C. Hopmann, A progressive damage model for unidirectional fibre reinforced composites with application to impact and penetration simulation, Appl. Compos. Mater. 23 (3) (2016) 495–522, https://doi.org/10.1007/s10443-015-9470-3

[36] J. Wiegand, Constitutive Modelling of Composite Materials Under Impact Loading ((Ph.D. thesis)), Oxford University, UK, 2009.

[37] Z. Zhai, B. Jiang, D. Drummer, Nonlinear material model for quasi-unidirectional woven composite accounting for viscoelastic, viscous deformation, and stiffness reduction, Polymers 10 (8) (2018) https://doi.org/10.3390/polym10080903

[38] M. Zscheyge, R. Böhm, A. Hornig, J. Gerritzen, M. Gude, Rate dependent non-linear mechanical behaviour of continuous fibre-reinforced thermoplastic composites – experimental characterisation and viscoelastic-plastic damage modelling, Mater. Des. 193 (2020) 108827, https://doi.org/10.1016/j.matdes.2020.108827

[39] C. Andriß, A. Kenf, S. Schmeer, Experimental characterization and phenomenological modeling of nonlinear viscoelasticity, plasticity and damage of continuous carbon fiber-reinforced thermoplastics, Compos. Part B Eng. 259 (2023) 110734, https://doi.org/10.1016/j.compositesb.2023.110734, http://dx.doi.org/10.1016/j.compositesb.2023.110734.

[40] J. Popp, T. Kleffel, D. Römisch, T. Papke, M. Merklein, D. Drummer, Fiber orientation mechanism of continuous fiber reinforced thermoplastics hybrid parts joined with metallic pins, Appl. Compos. Mater. (Apr 2021) https://doi.org/10.1007/s10443-021-09892-0.

[41] J. Popp, D. Drummer, Joining of continuous fiber reinforced thermoplastic/steel hybrid parts via undercutting pin structures and infrared heating, J. Adv. Join. Process. 5 (2022) 100084, https://doi.org/10.1016/j.jajp.2021.100084

[42] B. Gröger, J. Gerritzen, A. Hornig, M. Gude, Developing a numerical modelling strategy for metallic pin pressing processes in fibre reinforced thermoplastics to investigate fibre rearrangement mechanisms during joining, Proc. Inst. Mech. Eng. Part L J. Mater. Des. Appl. 238 (12) (2024) 2286–2298, https://doi.org/10.1177/14644207241280035

[43] R. Gerlach, C.R. Siviour, J. Wiegand, N. Petrinic, In-plane and through-thickness properties, failure modes, damage and delamination in 3D woven carbon fibre composites subjected to impact loading, Compos. Sci. Technol. 72 (3) (2012) 397–411, https://doi.org/10.1016/j.compscitech.2011.11.032

[44] J. Wiegand, A. Hornig, R. Gerlach, C. Neale, N. Petrinic, W. Hufenbach, An experimental method for dynamic delamination analysis of composite materials by impact bending, Mech. Adv. Mater. Struct. 22 (5) (2014) 413–421, https://doi.org/10.1080/15376494.2012.736066

[45] I. Lapczyk, J.A. Hurtado, Progressive damage modeling in fiber-reinforced materials, Compos. Part A Appl. Sci. Manuf. 38 (11) (2007) 2333–2341, https://doi.org/10.1016/j.compositesa.2007.01.017

[46] L. Maio, E. Monaco, F. Ricci, L. Lecce, Simulation of low velocity impact on composite laminates with progressive failure analysis, Composite Struct. 103 (2013) 75–85, https://doi.org/10.1016/j.compstruct.2013.02.027

[47] Polypropylene bj100hp polypropylene copolymer, ed. 7 (Dec 2021Borealis AG). https://www.borealisgroup.com/storage/Datasheets/bj100hp/BJ100HP-PDS-REG_EUROPE-EN-V7-PDS-EUR-27865-10014097.pdf.

[48] D. Römisch, J. Popp, D. Drummer, M. Merklein, Joining of CFRT-steel hybrid parts via hole-forming and subsequent pin caulking, Prod. Eng. 16 (2–3) (2021) 339–352, https://doi.org/10.1007/s11740-021-01093-9

[49] J. Popp, D. Drummer, Influence of the textile reinforcement on the joint formation of pin-joined composite/metal parts, Appl. Compos. Mater. 31 (3) (2024) 799–822, https://doi.org/10.1007/s10443-024-10203-6

[50] H.A. Rijsdijk, M. Contant, A.A.J.M. Peijs, Continuous-glass-fibre-reinforced polypropylene composites. 1. Influence of maleic-anhydride-modified polypropylene on mechanical properties, Compos. Sci. Technol. 48 (1–4) (1993) 161–172.

[51] M. Nikforooz, M. Golzar, M.M. Shokrieh, J. Montesano, Processability and tensile performance of continuous glass fiber/polyamide laminates for structural load-bearing applications, Compos. Part A Appl. Sci. Manuf. 105 (2018) 156–164, https://doi.org/10.1016/j.compositesa.2017.11.010

[52] R. Böhm, M. Gude, W. Hufenbach, A phenomenologically based damage model for 2D and 3D-textile composites with non-crimp reinforcement, Mater. Des. 32 (5) (2011) 2532–2544, https://doi.org/10.1016/j.matdes.2011.01.049

[53] M. Kashtalyan, C. Soutis, Stiffness degradation in cross-ply laminates damaged by transverse cracking and splitting, Compos. Part A: Appl. Sci. Manuf. 31 (4) (2000) 335–351, https://doi.org/10.1016/S1359-835X(99)00077-9

[54] R.G. Cuntze, A. Freund, The predictive capability of failure mode concept-based strength criteria for multidirectional laminates, Compos. Sci. Technol. 64 (3–4) (2004) 343–377, https://doi.org/10.1016/S0266-3538(03)00218-5

[55] R.G. Cuntze, The predictive capability of failure mode concept-based strength criteria for multi-directional laminates—part b, Compos. Sci. Technol. 64 (3–4) (2004) 487–516, https://doi.org/10.1016/S0266-3538(03)00225-2

[56] R.G. Cuntze, Efficient 3D and 2D failure conditions for UD laminae and their application within the verification of the laminate design, Compos. Sci. Technol. 66 (7–8) (2006) 1081–1096, https://doi.org/10.1016/j.compscitech.2004.12.046

[57] R. Böhm, M. Gude, W. Hufenbach, A phenomenologically based damage model for textile composites with crimped reinforcement, Compos. Sci. Technol. 70 (1) (2010) 81–87, https://doi.org/10.1016/j.compscitech.2009.09.008

[58] R. Hill, A theory of the yielding and plastic flow of anisotropic metals, Proc. R. Soc. Lond. Ser. A Math. Phys. Sci. 193 (1948) 281–297.

[59] W.-F. Chen, D.J. Han, Plasticity for Structural Engineers, Springer, New York and Berlin and Heidelberg and London and Paris and Tokyo, 1988.

[60] W. Prager, Recent developments in the mathematical theory of plasticity, J. Appl. Phys. 20 (3) (1949) 235–241, https://doi.org/10.1063/1.1698348

[61] Din EN ISO 527-5: Plastics - determination of tensile properties - part 5: test conditions for unidirectional fibre-reinforced plastic composites (2010).

[62] Din EN ISO 14129: fibre-reinforced plastic composites - determination of the in-plane shear stress/strain response, including the in-plane shear modulus and strength by the ±45° (1998).

[63] S.R. Hallett, Three-point beam impact tests on T300/914 carbon-fibre composites, Compos. Sci. Technol. 60 (1) (2000) 115–124, https://doi.org/10.1016/s0266-3538(99)00099-8

[64] P. Virtanen, R. Gommers, T.E. Oliphant, M. Haberland, T. Reddy, D. Cournapeau, E. Burovski, P. Peterson, W. Weckesser, J. Bright, S.J. van der Walt, M. Brett, J. Wilson, K.J. Millman, N. Mayorov, A.R.J. Nelson, E. Jones, R. Kern, E. Larson, C.J. Carey, İ. Polat, Y. Feng, E.W. Moore, J. VanderPlas, D. Laxalde, J. Perktold, R. Cimrman, I. Henriksen, E.A. Quintero, C.R. Harris, A.M. Archibald, A.H. Ribeiro, F. Pedregosa, P. van Mulbregt, SciPy 1.0 Contributors, SciPy 1.0: fundamental algorithms for scientific computing in Python, Nat. Methods 17 (2020) 261–272, https://doi.org/10.1038/s41592-019-0686-2

[65] D.S.S. Corp, Abaqus/user's manual (2017) https://help.3ds.com/2022/English/DSSIMULIA_Established/SIMULIA_Established_FrontmatterMap/sim-r-DSDocAbaqus.htm?contextscope=all&redirect_lang=English.

[66] W. Hufenbach, A. Langkamp, A. Hornig, M. Zscheyge, R. Bochynek, Analysing and modelling the 3D shear damage behaviour of hybrid yarn textile-reinforced thermoplastic composites, Comp. Struct. 94 (1) (2011) 121–131, https://doi.org/10.1016/j.compstruct.2011.07.010

[67] M. Kuhtz, A. Hornig, M. Gude, H. Jäger, A method to control delaminations in composites for adjusted energy dissipation characteristics, Mater. Des. 123 (2017) 103–111, https://doi.org/10.1016/j.matdes.2017.03.003

[68] W.C. Cui, M.R. Wisnom, M. Jones, Failure mechanisms in three and four point short beam bending tests of unidirectional glass/epoxy, J. Strain Anal. Eng. Des. 27 (4) (1992) 235–243, https://doi.org/10.1243/03093247v274235

[69] A.I. Selmy, A.R. Elsesi, N.A. Azab, M.A. Abd El-Baky, Interlaminar shear behavior of unidirectional glass fiber (U)/random glass fiber (R)/epoxy hybrid and non-hybrid composite laminates, Compos. Part B: Eng. 43 (4) (2012) 1714–1719, https://doi.org/10.1016/j.compositesb.2012.01.031

[70] J. Gerritzen, A. Hornig, M. Gude, Efficient failure information propagation under complex stress states in fiber reinforced polymers: from micro- to meso-scale using machine learning, in: Sheet Metal 2025, vol. 52 of SheMet2025, Materials Research Forum LLC, 2025, pp. 260–267, http://dx.doi.org/10.21741/9781644903551-32.